

BSN-VI: Multiband Light Curve Modeling of Four W UMa-Type Contact Binaries

I. Revisiting Energy Transfer Mechanisms and Luminosity Behavior

ELHAM SARVARI,^{1,*} ATILA PORO,^{2,3,†} RAUL MICHEL,⁴ ANNA FRANCESCA PALA,⁵ MEHMET TANRIVER,^{6,7}
 AHMET BULUT,^{8,9} AHMET KESKIN,⁶ AND MARK G. BLACKFORD¹⁰

¹*BSN Project; Independent researcher, 12101 Berlin, Germany*

²*LUX, Observatoire de Paris, CNRS, PSL, 61 Avenue de l'Observatoire, 75014 Paris, France*

³*Department of Astronomy, Raderon AI Lab, Burnaby, British Columbia V5C 0J3, Canada*

⁴*Instituto de Astronomía, UNAM. A.P. 106, 22800 Ensenada, BC, México*

⁵*European Southern Observatory, Karl Schwarzschild Straße 2, D-85748 Garching, Germany*

⁶*Department of Astronomy and Space Science, Faculty of Science, Erciyes University, Kayseri TR-38039, Türkiye*

⁷*Erciyes University, Astronomy and Space Science Observatory Application and Research Center, Kayseri TR-38039, Türkiye*

⁸*Department of Physics, Faculty of Arts and Sciences, Çanakkale Onsekiz Mart University, Terzioğlu Kampüsü, TR-17020, Çanakkale, Türkiye*

⁹*Astrophysics Research Center and Observatory, Çanakkale Onsekiz Mart University, Terzioğlu Kampüsü, TR-17020, Çanakkale, Türkiye*

¹⁰*Variable Stars South (VSS), Congarinni Observatory, Congarinni, NSW, 2447, Australia*

ABSTRACT

We presented the first high-precision, detailed photometric analysis of four W Ursae Majoris (W UMa)-type contact binaries, Linear 10772300, Linear 11150338, Linear 20372537 and DM Cir. In addition to ground-based multiband photometric observations, data from the Transiting Exoplanet Survey Satellite (TESS) were employed for the analysis of the DM Cir system. New ephemeris and linear fit to the O–C diagrams were derived using extracted times of minima and additional literature. The light curve modeling was performed using the PHysics Of Eclipsing BinariEs (PHOEBE) Python code and the BSN application, employing a Markov Chain Monte Carlo approach. In each systems, the two stellar components exhibited minimal temperature differences ($\Delta T < 150$ K), confirming efficient energy exchange within their common convective envelopes. Absolute parameters were estimated using the Gaia Data Release 3 (Gaia DR3) parallax and astrophysical equations. Based on effective temperatures and component masses, two systems were classified as W-subtype systems, while others belonged to the A-subtype. We computed the initial masses of the primary (M_{1i}) and secondary (M_{2i}) components for four target systems using a method based on the observational properties of overluminous secondary components. We found initial primary masses in the range 0.6 – $1.0 M_{\odot}$ and initial secondary masses in the range 0.9 – $1.7 M_{\odot}$ with mass loss $< 1.0 M_{\odot}$. We investigated the relative energy transfer rates (U_1 and U_2) and nuclear luminosities (L_{10} and L_{20}) based on the physical parameters of 411 W UMa-type contact binaries, including the four systems analyzed in this study, through wide range of mass ratios. The results for all systems provided a comprehensive view of energy transfer behavior throughout different evolutionary stages of contact binaries.

Keywords: Eclipsing binary stars - Fundamental parameters of stars - Astronomy data analysis - Individual (Four contact binary stars)

1. INTRODUCTION

Binary stars play a fundamental role in astrophysics, not only because they are numerous, but also because they serve as a primary source of our knowledge about the fundamental properties of stars (Kallrath et al. 2009; Latham et al. 1992). Observational studies indicate that more than half of the stars in the solar neighborhood belong to binary or multiple systems (Kallrath et al. 2009). Binary systems are characterized by measurable gravitational interactions

* First author: elham.sarvari@aei.mpg.de

† Corresponding author: atilaporo@bsnp.info, atila.poro@obspm.fr

that allow stellar parameters to be estimated. Orbital motion produces detectable variations in position and velocity over a wide range of stellar separations and luminosity ratios, allowing both stars to be studied in detail depending on their distances, brightnesses, and motions (Latham et al. 2002).

Eclipsing binary systems are especially valuable in this context, as their orbital planes are oriented edge-on to the observer, allowing eclipses to occur. W UMa systems are a subclass of eclipsing binaries in which both stars fill their inner Lagrangian surfaces (usually referred to as Roche Lobes), and share a common convective envelope (Lucy 1968a). If the components fill their Roche lobes, the system is classified as a contact binary, and its degree of filling can be quantified by the filling factor (Wilson 2001). W UMa systems are commonly divided into two subclasses: A and W subtypes. In A-subtype systems, the more massive star is hotter; whereas in W-subtype systems, the more massive star is cooler than its companion (Binnendijk 1970; Poro et al. 2026b). Both subclasses are characterized by continuously varying light curves, with only a small difference between the depths of the minima. The nearly equal depths of the two minima indicate that, despite their different masses, both components have nearly identical temperatures (Qian et al. 2014). However, some systems exhibit notable asymmetries—such as the O’Connell effect O’Connell (1951), where the two maxima differ in brightness. Such asymmetries are more frequently observed in W-subtype systems (Kallrath et al. 2009).

Despite extensive studies, W UMa-type contact binary systems remain under active investigation, and precise observations and analysis are crucial for understanding their structure and evolution (Rahunen & Vilhu 1982). Establishing a consistent theoretical framework for these systems is challenging, as their evolution is governed by the coupled effects of mass and energy transfer, angular momentum loss (AML), and the requirement to maintain an apparent thermal equilibrium at the stellar surfaces (Li et al. 2004; Stepień 2005). These processes operate on different timescales and are not directly constrained by observations, leading to degeneracies among model parameters and complicating the interpretation of observed systems. Moreover, the evolutionary states of the components are often assessed or compared using single-star evolutionary models, despite the fact that ongoing interaction between the components can significantly alter their internal structure and evolutionary paths (Gazeas & Stepień 2008).

This study presents ground-based, multiband photometric observations of four W UMa-type contact binaries, with the aim of conducting a detailed photometric analysis. It continues the investigation initiated by Poro et al. (2025c), Poro et al. (2025d), and Poro et al. (2025b) by conducting new observations and a comprehensive analysis of W UMa-type contact binary systems in the BSN project¹. The structure of this paper is organized as follows: Section 2 provides details about the target systems. Section 3 describes the ground-based observations and the data reduction process. Section 4 presents the determination of a new ephemeris, while Section 5 includes the photometric light curve analysis for the target systems. Section 6 outlines the methods used to determine the absolute parameters. Finally, Section 7 offers a discussion and conclusions.

2. TARGET SYSTEMS

We investigated four binary star systems: Linear 10772300 (hereinafter L10772300), Linear 11150338 (hereinafter L11150338), Linear 20372537 (hereinafter L20372537), and DM Cir. These systems are classified as contact binaries in both the All-Sky Automated Survey for SuperNovae (ASAS-SN; Shappee et al. 2014; Jayasinghe et al. 2018) and the AAVSO Variable Star Index (VSX²) catalogs. Table 1 presents some specifications of the target systems as listed in the Gaia DR3³ catalog. Table 2 provides the observation characteristics for each system, including the observation date, filters, exposure time, and the name of the observatory. In each case, we utilized V_{\max} derived from our observations. Brief introductions to the targets are provided below.

- L10772300: The binary system L10772300 was discovered by the Lincoln Near-Earth Asteroid Research (LINEAR) project and included in the LINEAR III Catalog of Periodic Variables (Palaversa et al. 2013). In addition to ASAS-SN and VSX, it is also classified as a contact binary in several other catalogs, including the Catalina Surveys catalog of periodic variable stars (CRTS; Drake et al. 2014), the TESS Input Catalog version 8.2 (TIC; Paegert et al. 2021), the Sloan Digital Sky Survey (SDSS; Ahumada et al. 2020), and the Zwicky Transient Facility (ZTF; Bellm et al. 2019). The orbital period is 0.244452 days, while the effective temperature is reported as 5233 K in Gaia DR3 and 5138 ± 153 K in the TIC.

¹ <https://bsnp.info>

² <https://vsx.aavso.org/>

³ <https://www.cosmos.esa.int/web/gaia/data-release-3>

Table 1. General parameters of the target systems, including coordinates, distances, and orbital periods.

System	TIC	RA. $^{\circ}$ (J2000)	DEC. $^{\circ}$ (J2000)	d(pc)	P_d (day)
L10772300	23871740	211.7077137	40.7781799	1292(59)	0.244452(VSX)
L11150338	138186324	212.1970867	35.3223105	2151(126)	0.314730(VSX)
L20372537	101717663	259.8652614	36.2387627	1252(139)	0.288766(VSX)
DM Cir	47309500	231.0349806	-56.8376572	163(1)	0.386777(ASAS-SN)

- L11150338: It is part of the LINEAR III survey’s sample of variable stars spanning 10,000 deg^2 of the northern sky. An orbital period of 0.314730 days has been reported by both the VSX catalog and the catalog of contact binaries in LAMOST DR7 (Qian et al. 2020), while the time of minimum is available from the ASAS-SN catalog. The effective temperature of the system is reported as 6048 K by Gaia DR3 and 5980 ± 87 K by the TIC.
- L20372537: The ZTF Variable Stars Catalog and the VSX catalog report orbital periods of 0.2887654 and 0.288760 days, respectively. The TIC catalog reports an effective temperature of 4661 ± 154 K for this system.
- DM Cir: Houk, N., & Cowley, A. P. (1975) reported this system as a new variable from the Southern hemisphere for the first time. The orbital period of DM Cir is reported as 0.386777 days in the ASAS catalog of eclipsing binaries with RASS counterparts (Szczygiel et al. 2008), 0.3867749 days in the General Catalogue of Variable Stars (GCVS; Malkov et al. 2006), 0.386773 days in the VSX catalog, and 0.3868075 days in the TESS.

3. OBSERVATION AND DATA REDUCTION

Photometric observations and data reduction procedures were conducted using standard filters for four target systems at two observatories located in the Northern and Southern Hemispheres. Three of the systems were observed at the San Pedro Mártir Observatory (SPM) in México, while the remaining system was observed at the Congarinni Observatory in Australia. Among the targets, DM Cir was the only system with available timeseries data from TESS (Ricker et al. 2010, Stassun et al. 2018). The observational details, including dates, filters, and exposure times, are provided in Table 2, while the characteristics of the comparison and check stars used during the observations are summarized in Table 3. A detailed description of the observational facilities is presented in the following section.

3.1. SPM Observatory

The three binary systems L10772300, L11150338, and L20372537 were observed at the San Pedro Mártir (SPM) Observatory in México. This observatory is located at a longitude of $115^{\circ} 27' 49''$ W, latitude $31^{\circ} 02' 39''$ N, and an altitude of 2830 meters above sea level. Observations were conducted using a 1.5-meter telescope equipped with the RUCA filter wheel and a Spectral Instruments CCD camera. The detector consists of an e2v CCD42-40 chip with $13.5 \times 13.5 \mu m^2$ pixels, a gain of $1.39e^-ADU^{-1}$, and a readout noise of $3.54 e^-$. Standard Johnson–Cousins B , V , R_c , and I_c filters were employed during the observations. Photometric image processing was performed using standard IRAF routines (Tody 1986), and data reduction was carried out using bias subtraction and flat-field correction.

3.2. Congarinni Observatory

Photometric observations of DM Cir were conducted in June 2019 and May 2020 using standard B , V , and I_c filters. These observations were performed with an Orion ED80T CF refractor telescope at the Congarinni Observatory in Australia, located at longitude $152^{\circ} 52'$ E and latitude $30^{\circ} 44'$ S. An Atik One 6.0 CCD camera was used with 1×1 binning. Exposure times were set to 30 seconds for the B filter and 12 seconds for both the V and I_c filters. A total of 1935 images were acquired in the BVI_c filters throughout the observational campaign.

3.3. TESS Observations

NASA launched the TESS Satellite in 2018 to discover TESS, equipped with four wide-field cameras, systematically observes different regions of the sky, dedicating 27.4 days to each sector. In this study, time-series photometric data from TESS were available only for the DM Cir system, as comparable data were not available for the other three targets. Observations from Sectors 38, 39, and 65, obtained in 2021 and 2023, were used. Sectors 38 and 39 were

Table 2. Specifications of the ground-based observations.

System	Observation(s) Date	Filter	Exposure time(s)	Observatory
L10772300	2024(May7)	BVR_cI_c	$B(60), V(30), R_c(20), I_c(20)$	SPM
L11150338	2024(May13)	BVR_cI_c	$B(30), V(15), R_c(10), I_c(10)$	SPM
L20372537	2024(June17)	BVR_cI_c	$B(60), V(30), R_c(20), I_c(15)$	SPM
DM Cir	2019(June19,21,22), 2020(May10,11)	BVI_c	$B(30), V(12), I_c(12)$	Congarinni

Table 3. List the comparisons and check stars in the ground-based observations. Coordinates come from the Gaia DR3.

System	Star Type	RA. $^{\circ}$ (J2000)	DEC. $^{\circ}$ (J2000)
L10772300	Comparison	211.713538	40.808615
L10772300	Check	211.695935	40.778505
L11150338	Comparison	212.190099	35.291748
L11150338	Check	212.246209	35.324273
L20372537	Comparison	259.927774	36.257595
L20372537	Check	259.861978	36.255877
DM Cir	Comparison	231.010255	-56.676385
DM Cir	Check	231.057119	-56.699295

observed with an exposure time of 600 seconds, while Sector 65 used a shorter exposure time of 200 seconds. The times of minima extracted from these TESS sectors for DM Cir are presented in Table A1. All data were retrieved from the Mikulski Archive for Space Telescopes (MAST)⁴, and the light curves were detrended using the SPOC pipeline.

4. NEW EPHEMERIS

The primary and secondary minima of all four systems were extracted from our ground-based observations with standard B , V , R_c , and I_c filters. They were also combined with 408 mid-eclipse times extracted from three time-series TESS sector data, complemented by additional minima collected from the literature for the subsequent calculations. Since the times of minima were reported in both Barycentric Julian Date in Barycentric Dynamical Time (BJD_{TDB}) and Heliocentric Julian Date (HJD), we first converted all minima times to BJD_{TDB} using an online converter⁵ (Eastman et al. 2010). Gaussian curve fitting was applied to derive the precise times of minima. The extracted times of minima are listed in Table 4. Additionally, mid-eclipse times from the TESS data in sectors 38, 39, and 65 (observed in 2021 and 2023) for DM Cir are listed in Appendix Table A1.

In binary star systems, the Observed–Calculated (O–C) diagram is an essential tool for refining and updating the system’s ephemeris. In this study, a linear fit is more appropriate for the O–C diagrams, given the limited number of observations and minima available for our four binary systems. The O–C diagrams are presented in Figure 1. For each system, the epoch and O–C values were calculated using the ephemeris references listed in Table 5. The O–C values were calculated based on the linear ephemeris

$$BJD(E) = BJD_0 + P \times E, \quad (1)$$

where $BJD(E)$ denotes the predicted eclipse time at epoch E , BJD_0 is the reference epoch, and P represents the orbital period. For L10772300 and L11150338, we used minima from our ground-based observations and orbital periods reported in the VSX catalog. For L20372537, the reference ephemeris was determined using a minimum time

⁴ <https://mast.stsci.edu/portal/Mashup/Clients/Mast/Portal.html>

⁵ <https://astroutils.astronomy.osu.edu/time/hjd2bjd.html>

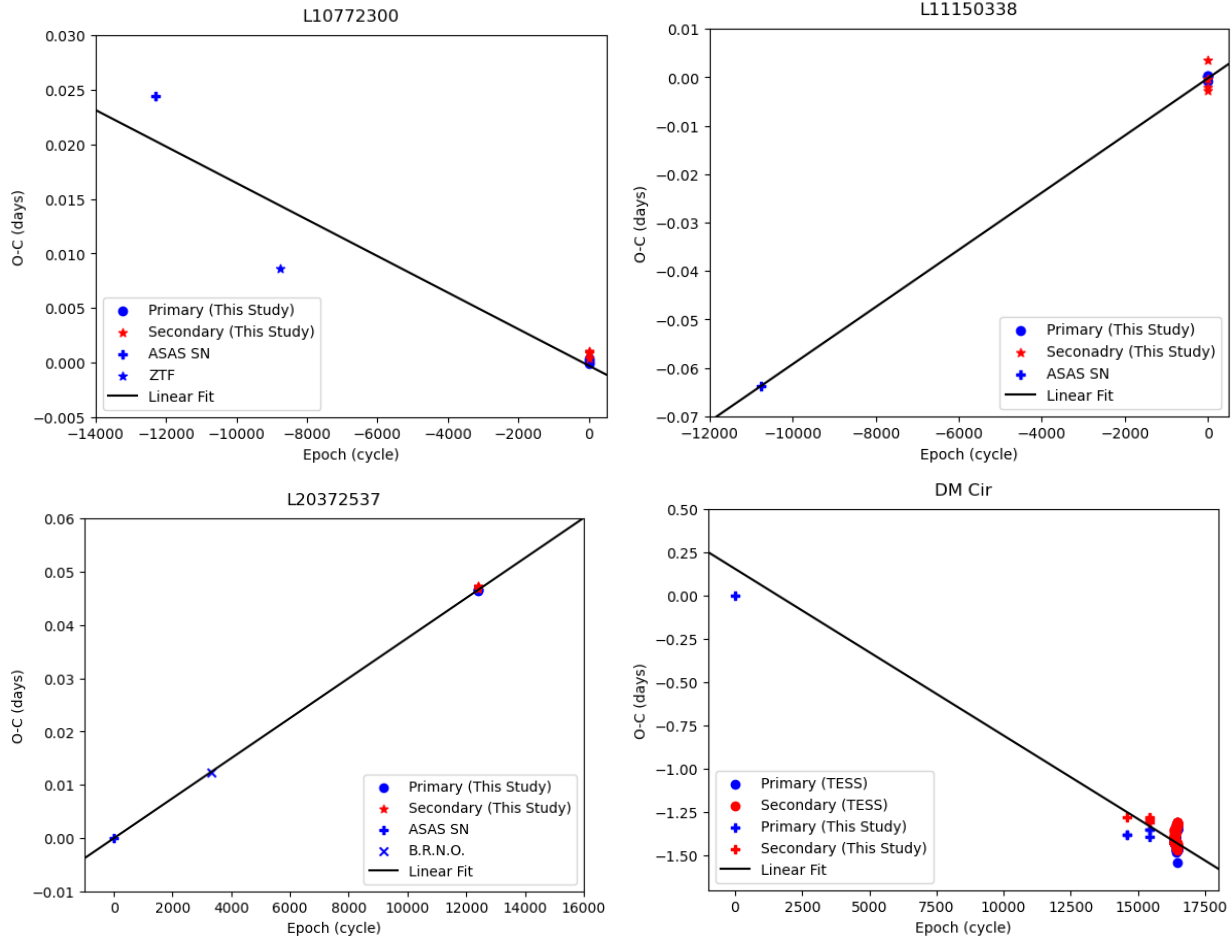


Figure 1. O–C diagrams illustrating the period variations of the targets.

from [Jayasinghe et al. \(2019\)](#) and a period from the ASAS-SN catalog. For DM Cir, both the minimum and period were taken from [Otero & Claus \(2004\)](#). The new ephemeris for each system is presented in Table 5.

5. LIGHT CURVE SOLUTIONS

The light curve solution process was initiated by converting the time into orbital phase, using the new ephemeris listed in Table 5. The analysis of contact binary systems was then conducted using PHOEBE version 2.4.9, a Python-based modeling tool [Prša & Zwitter \(2005\)](#); [Prša et al. \(2016\)](#); [Conroy et al. \(2020\)](#), together with the BSN application version 1.0 [Paki et al. \(2025\)](#) offered by the BSN project, and Markov chain Monte Carlo (MCMC) approach ([Prša et al. 2016](#)). This work provides the first photometric light curve solutions of the four target systems, which have not previously been studied in the literature. The contact binary systems approach was utilized based on catalog classifications and further supported by the short orbital periods along with the morphological features of the light curves. The initial modeling of each target system was conducted using the PHOEBE code, which employs built-in optimization algorithms to estimate parameters before applying the MCMC approach. In all models, the bolometric albedos and gravity-darkening coefficients were set to $A_1 = A_2 = 0.5$ ([Rucinski 1969](#)) and $g_1 = g_2 = 0.32$ ([Lucy 1967](#)), respectively. The stellar atmospheres were modeled based on [Castelli & Kurucz \(2004\)](#) study, while the limb darkening coefficients were treated as free parameters.

The initial components' effective temperatures for three binary systems, L10772300, L11150338, and DM Cir, were obtained from Gaia DR3. As Gaia DR3 does not provide this information for L20372537, its temperature was instead obtained from the MAST archive with source information from TIC version 8.2. In all cases, the initial temperature was placed in the hotter component, based on the depths of the light curve minima. The effective temperature of the

Table 4. The times of minima for four target systems from both the literature and this study

System	Min.(BJD_{TDB})	Error	Filter	Epoch	O-C	Reference
L10772300	2457433.02001			-12296	0.0244	ASAS-SN
	2458295.18642			-8769	0.0086	ZTF
	2460438.77773	0.00019	<i>B</i>	0	0.0003	This study
	2460438.77739	0.00016	<i>I</i>	0	0	This study
	2460438.77761	0.00016	<i>R</i>	0	0.0002	This study
	2460438.77732	0.00013	<i>V</i>	0	-0.0001	This study
	2460438.89997	0.00031	<i>B</i>	0.5	0.0004	This study
	2460438.90058	0.00018	<i>I</i>	0.5	0.0010	This study
	2460438.90063	0.00014	<i>R</i>	0.5	0.0010	This study
	2460438.90048	0.00010	<i>V</i>	0.5	0.0009	This study
L11150338	2457061.053915			-10751	-0.0637	ASAS-SN
	2460444.78019	0.00029	<i>B</i>	0	0.0004	This study
	2460444.77897	0.00046	<i>I</i>	0	-0.0009	This study
	2460444.77983	0.00031	<i>R</i>	0	0	This study
	2460444.78014	0.00023	<i>V</i>	0	0.0003	This study
	2460444.94065	0.00120	<i>B</i>	0.5	0.0035	This study
	2460444.93435	0.00227	<i>I</i>	0.5	-0.0028	This study
	2460444.93520	0.00149	<i>R</i>	0.5	-0.0020	This study
	2460444.93684	0.00141	<i>V</i>	0.5	-0.0004	This study
L20372537	2456900.79026			0	0	ASAS-SN
	2457856.59818	0.00001		3310	0.0123	VarAstro
	2460479.72839	0.00015	<i>B</i>	12394	0.0467	This study
	2460479.72801	0.00009	<i>I</i>	12394	0.0463	This study
	2460479.72832	0.00011	<i>R</i>	12394	0.0466	This study
	2460479.72826	0.00008	<i>V</i>	12394	0.0466	This study
	2460479.87293	0.00019	<i>B</i>	12394.5	0.0469	This study
	2460479.87320	0.00013	<i>I</i>	12394.5	0.0471	This study
	2460479.87329	0.00034	<i>R</i>	12394.5	0.0472	This study
	2460479.87332	0.00014	<i>V</i>	12394.5	0.0472	This study
DM Cir	2458654.13468	0.00024	<i>V</i>	14588	-0.0199	This study
	2458656.06857	0.00018	<i>V</i>	14593	-0.0199	This study
	2458657.03693	0.00036	<i>V</i>	14595.5	-0.0185	This study
	2458980.96116	0.00024	<i>V</i>	15433	-0.0200	This study
	2458980.96169	0.00026	<i>B</i>	15433	-0.0195	This study
	2458980.96183	0.00025	<i>I</i>	15433	-0.0194	This study
	2458981.15578	0.00025	<i>V</i>	15433.5	-0.0188	This study
	2458981.15602	0.00021	<i>B</i>	15433.5	-0.0186	This study
	2458981.15618	0.00030	<i>I</i>	15433.5	-0.0184	This study

Table 5. Reference and updated ephemerides of the four target systems.

System	Reference Ephemeris	updated Ephemeris
L10772300	$2460438.77739 + 0.244452 \times E$	$2460438.77710(177) + 0.2444503(3) \times E$
L11150338	$2460444.77983 + 0.314730 \times E$	$2460444.77978(28) + 0.31473592(6) \times E$
L20372537	$2456900.79026 + 0.288760 \times E$	$2456900.79021(12) + 0.28876376(1) \times E$
DM Cir	$2453011.85175 + 0.386777 \times E$	$2453011.85946(16) + 0.38677526(1) \times E$

cooler component was estimated using the difference in depth between the primary and secondary minima of the light curves.

The mass ratios $q = M_2/M_1$ of the systems were determined using the q -search method, based on photometric observations and following standard procedures (Terrell & Wilson 2005). An initial range of $q = 0.1$ to $q = 20$ was explored for all targets. Based on the minima in the sum of squared residuals, the interval was subsequently narrowed for a more refined analysis. As shown in Figure 2, each q -search curve exhibits a well-defined minimum, indicating the optimal mass ratio.

Our observations reveal an unequal brightness between the primary and secondary maxima in L10772300 and DM Cir target systems. Both cool and hot starspot configurations were examined on the secondary component in order to reproduce the observed light curve asymmetry. A cool starspot was ultimately adopted in the final light curve modeling, as it provided a better fit according to the reduced χ^2 statistic. The most probable explanation for this asymmetry in the light curve's maxima is that the magnetic activity of the components is causing the presence of the starspot(s), which are introduced with the O'Connell effect (O'Connell 1951). Other explanations for the O'Connell effect have also been proposed (Zhou & Leung e.g., 1990; Liu & Yang e.g., 2003; Fabry & Prša e.g., 2025a), addressing different possible mechanisms such as mass transfer. Starspots are generally categorized as cold or hot based on their relative temperature to the stellar photosphere. In light curve modeling, whether to use a cold- or a hot-starspot depends on which process (photospheric magnetic fields or mass exchange between components) most consistently explains the physical causes of the O'Connell effect (Knote et al. 2022; Kouzuma 2019). Cool spots, often found on late-type secondary components, are generally attributed to photospheric magnetic fields. According to dynamo theory Moss (2004), magnetic energy is generated by the conversion of kinetic energy that comes from convection in the outer layer. On the other hand, if a hot spot is considered in the modeling, it results from the impact of mass transfer between the components rather than from magnetic activity (Park et al. 2013). This scenario is more likely in contact and semi-detached systems, where at least one star fills its Roche lobe (Kouzuma 2019). Colatitude ($Col.^{\circ}$), longitude ($Long.^{\circ}$), angular radius ($Radius.^{\circ}$), and the ratio of temperature (T_{spot}/T_{star}) are the characteristics that are identified for a starspot (Table 6).

Next, we aimed to determine an acceptable theoretical fit for the observational data by utilizing the initial values. Additionally, we employed PHOEBE's optimization tools to refine the light curve solutions, using the same configuration described earlier. This allowed us to generate the results needed for the subsequent analysis step. We applied the high-speed MCMC algorithm implemented in the BSN application to refine the light curve solutions. This approach allowed us to derive the final results along with their associated uncertainties.

The BSN application is well-suited for this analysis, as its procedures are consistent with the PHOEBE standard program and produce numerically agreement results (Paki et al. 2025). Both the PHOEBE code and BSN utilize the emcee package Goodman & Weare (2010) for MCMC computations; however, the BSN application significantly improves MCMC performance. Thanks to its implementation in modern .NET technologies, this application generates synthetic light curves over 40 times faster than PHOEBE. This performance advantage is maintained despite methodological differences. Both BSN and PHOEBE discretize the Roche geometry using surface meshes; however, BSN follows the formulation of Mochnacki (1984), while PHOEBE adopts a Wilson–Devinney-based surface parametrization scheme (Wilson & Devinney 1971). The MCMC process in the BSN application operates based on five main parameters, T_1 , T_2 , q , f , and i . We employed 24 walkers and 1500 iterations to sample these parameters effectively. The third light component (l_3), representing a possible luminous contribution from the third component to the system's total flux, was found to be insignificant. For each of the four systems analyzed, the best theoretical fit to the

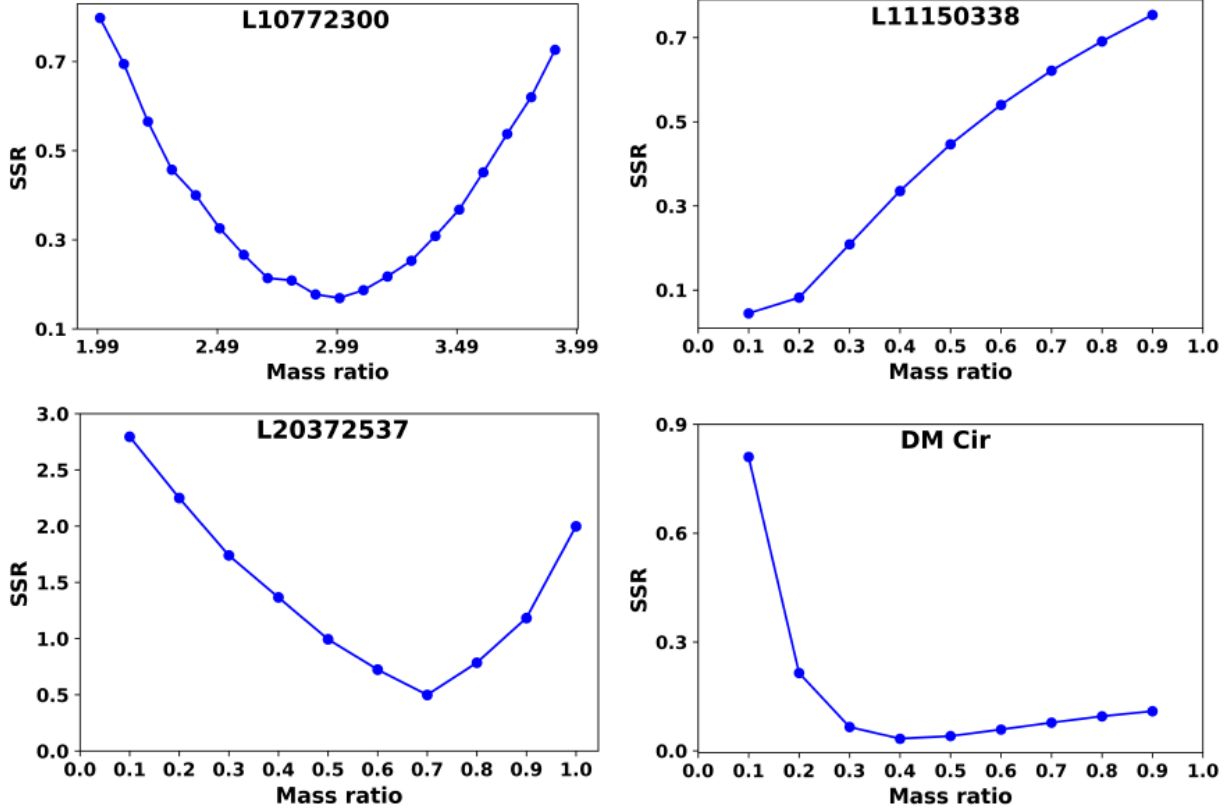


Figure 2. Sum of the squared residuals as a function of the mass ratio.

observational data was obtained without including this additional component, indicating no detectable evidence of a third star contributing to the system's luminosity.

The Figure 3 shows the corner plots based on the heat-map for targets, providing a visual representation of parameter distributions from MCMC analysis. Table 6 presents the final results of the light curve modeling along with their uncertainties. Figure 4 shows the observed and theoretical light curves in different filters. Additionally, Figure 5 illustrates the three-dimensional (3D) structure of the binary systems and the starspots on the stars. The color in the figure represents the variations in effective temperature across the stellar surfaces.

6. ABSOLUTE PARAMETERS

One possible method for estimating the absolute parameters of contact binary systems, where only photometric data are available, is to use the Gaia DR3 parallax, as thoroughly discussed in the study by Poro et al. (2024b). Estimating absolute parameters with the Gaia DR3 parallax method has certain limitations and requires an extinction coefficient (A_V) value lower than approximately 0.4 (Poro et al. 2024a). We estimated the A_V for four systems based on the 3D dust-map Python package and Gaia DR3 distance data (Green et al. 2019). The results were in an acceptable state for using the Gaia DR3 parallax method to determine the absolute parameters of the stars.

The V_{max} for each of the four systems was obtained from our ground-based observations and listed in Table 7. Also, the bolometric correction (BC) was estimated using the method provided by the Flower (1996) study. Estimating the system's parameters requires several inputs, including the distance from Gaia DR3, A_V , V_{max} , $l_{1,2}/l_{tot}$, $BC_{1,2}$, $T_{1,2}$, $r_{mean_{1,2}}$, and P . With these parameters, we can determine $M_{V_{1,2}}$, $M_{bol_{1,2}}$, $R_{1,2}$, $L_{1,2}$, $a_{1,2}$, and $M_{1,2}$. First, the method determined the absolute magnitude of the star (M_V) by using the apparent magnitude in the BVR_cI_c filter, the distance from Gaia DR3 (d) in parsecs, and A_V . Subsequently, using the $l_{1,2}/l_{tot}$ parameter obtained from the standard filters in the light curve solutions process, $M_{V_{1,2}}$ are calculated. The bolometric correction was applied to derive the bolometric absolute magnitude (M_{bol}) for each star.

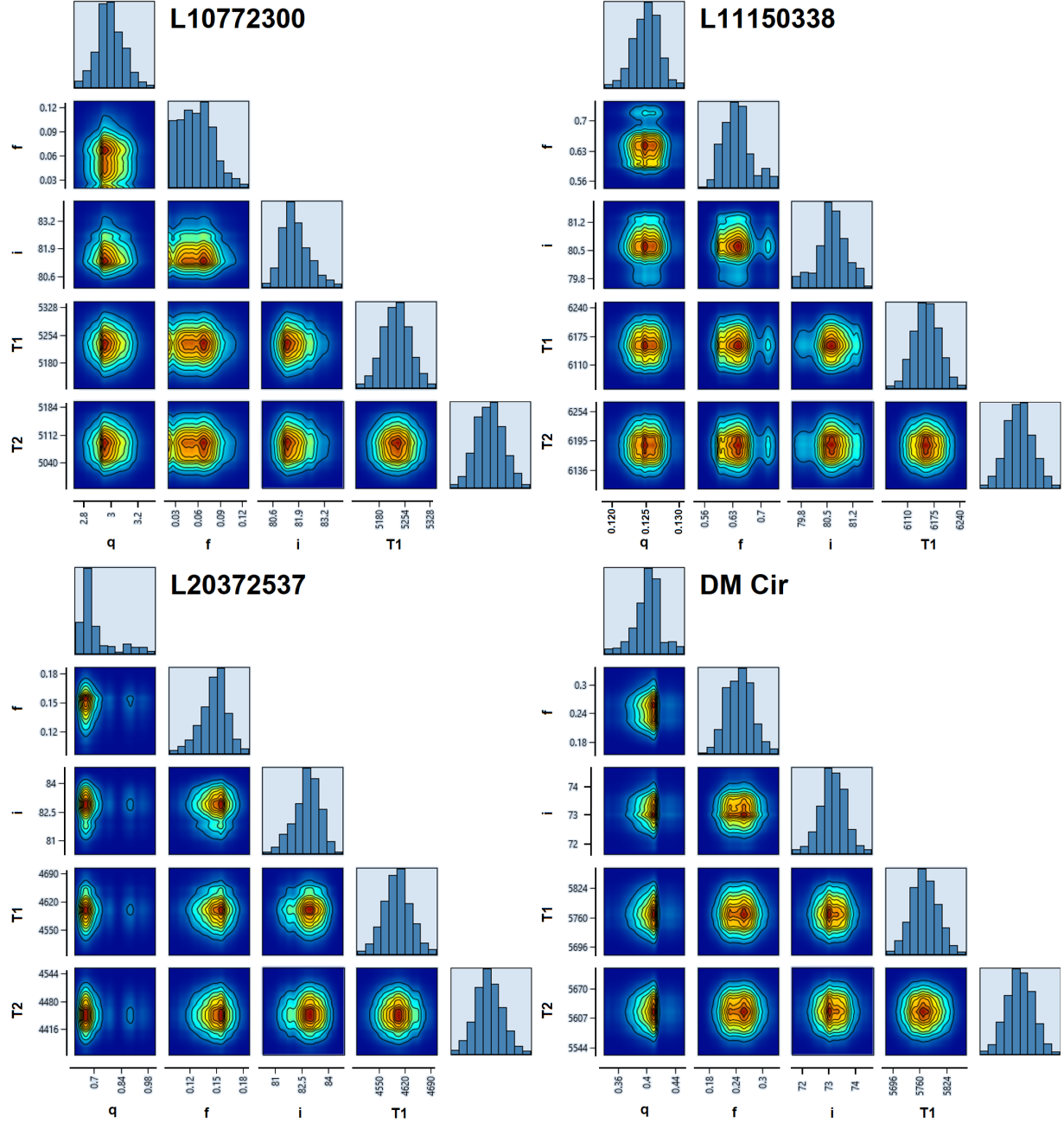


Figure 3. Corner plots based on the heat-map of the target contact binary systems were determined through MCMC modeling by the BSN application.

The radius of each star in the binary systems can be estimated through the relationship between M_{bol} and luminosity (L). Once L is derived and T is known, the radius (R) of each star can then be estimated. The semi-major axis $a(R_\odot)$ of each system is then derived using $R_{1,2}$, $r_{mean1,2}$, and averaging $a_1(R_\odot)$ and $a_2(R_\odot)$. The individual component masses can be determined by applying Kepler's third law, using the values of $a(R_\odot)$, P_{orb} , and q , as formulated in Equations 2 and 3.

$$M_1 = \frac{4\pi^2 a^3}{GP^2(1+q)}, \quad (2)$$

$$M_2 = q \times M_1. \quad (3)$$

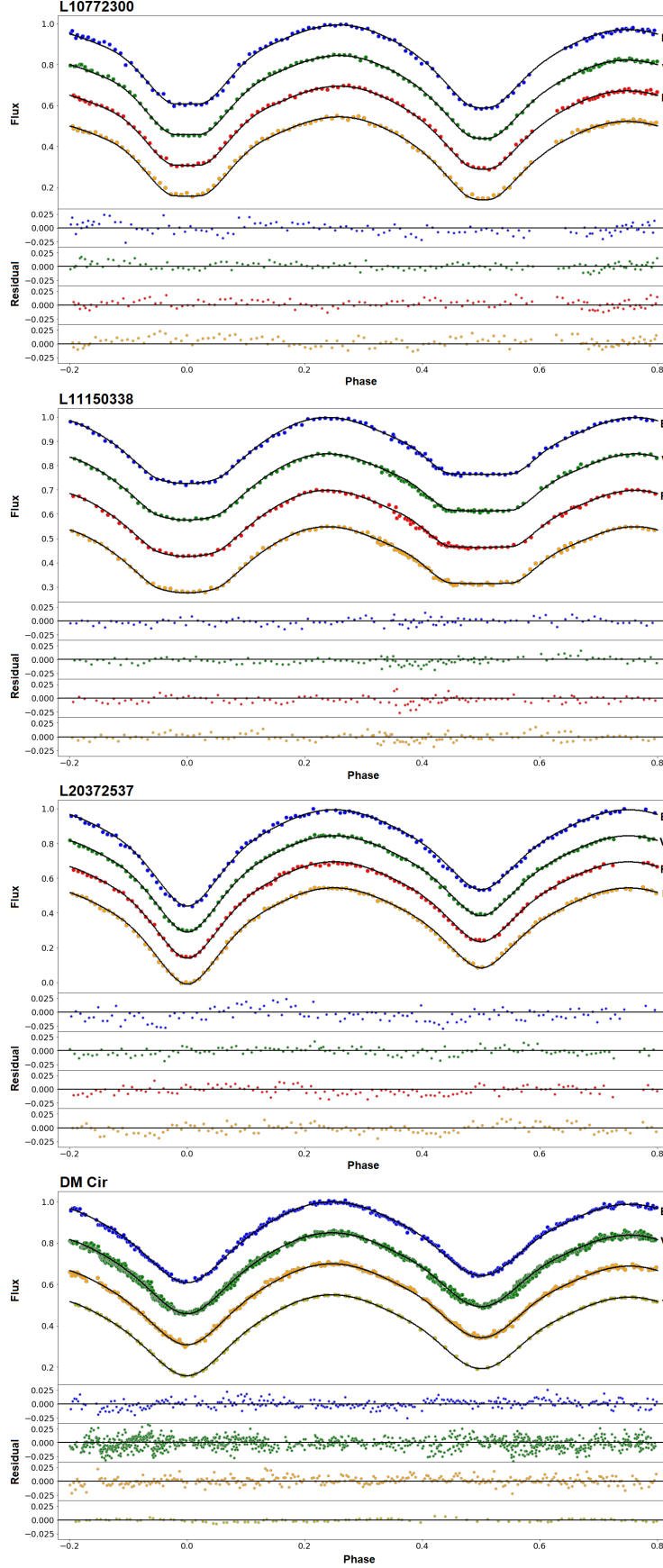
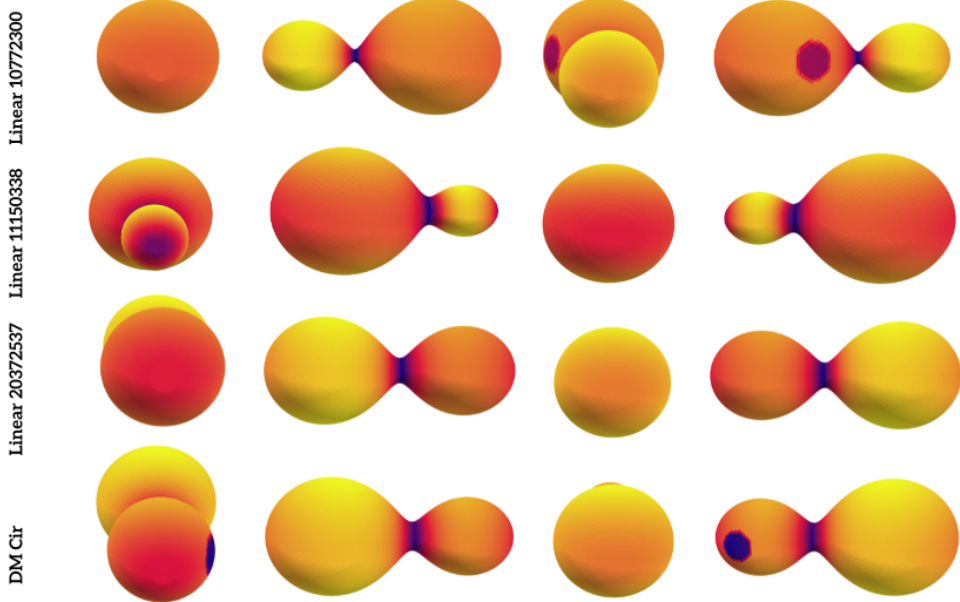


Figure 4. The colored dots represent the observed light curves of the systems in different filters, and the synthetic light curves, generated using the light curve solutions, are also shown. Residuals are shown at the bottom of each panel.

Table 6. Photometric solutions for the four target systems derived from light curve modeling.

Parameter	L10772300	L11150338	L20372537	DM Cir
T_1 (K)	5225(38)	6155(33)	4595(35)	5770(32)
T_2 (K)	5082(36)	6185(29)	4446(32)	5622(31)
$q = M_2/M_1$	2.992(101)	0.124(2)	0.669(71)	0.403(19)
i°	81.63(67)	80.63(36)	82.86(77)	73.21(51)
f	0.057(22)	0.640(34)	0.147(15)	0.250(31)
$\Omega_1 = \Omega_2$	6.570(311)	1.979(34)	3.131(259)	2.622(35)
l_1/l_{tot}	0.295(20)	0.857(18)	0.643(36)	0.719(6)
l_2/l_{tot}	0.705(20)	0.143(18)	0.357(36)	0.281(6)
$r_{1(mean)}$	0.291(2)	0.585(4)	0.428(7)	0.476(4)
$r_{2(mean)}$	0.480(1)	0.246(4)	0.357(7)	0.319(4)
$Col.spot$ (deg)	95(1)			92(1)
$Long.spot$ (deg)	302(2)			245(2)
$Rad.spot$ (deg)	16(1)			20(1)
T_{spot}/T_{star}	0.92(1)			0.90(1)
Component	Secondary			Secondary

**Figure 5.** 3D view of the stellar components in the four target binary systems at orbital phases 0, 0.25, 0.50, and 0.75, respectively.

Furthermore, the orbital angular momentum (J_0) of the systems was calculated using Equation 4 from [Eker et al. \(2006\)](#), where q represents the mass ratio, M is the total system mass, P is the orbital period, and G is the gravitational constant.

$$J_0 = \frac{q}{(1+q)^2} \sqrt[3]{\frac{G^2}{2\pi} M^5 P}. \quad (4)$$

The estimated absolute parameters derived for the four target systems are listed in Table 7.

Table 7. Absolute parameter estimation for the four target systems using Gaia DR3 parallaxes and astrophysical relations.

Parameter	L10772300	L11150338	L20372537	DM Cir
$M_1(M_\odot)$	0.40(11)	1.16(27)	1.08(44)	1.10(12)
$M_2(M_\odot)$	1.20(31)	0.14(3)	0.73(30)	0.44(5)
$R_1(R_\odot)$	0.56(5)	1.27(15)	0.96(15)	1.23(6)
$R_2(R_\odot)$	0.93(9)	0.51(3)	0.80(11)	0.82(4)
$L_1(L_\odot)$	0.21(3)	2.07(44)	0.37(11)	1.50(12)
$L_2(L_\odot)$	0.52(9)	0.34(4)	0.23(5)	0.61(4)
$M_{bol1}(\text{mag})$	6.45(14)	3.95(23)	5.83(31)	4.30(8)
$M_{bol2}(\text{mag})$	5.46(19)	5.90(11)	6.36(26)	5.29(7)
$\log g_1(\text{cgs})$	4.55(18)	4.30(20)	4.51(31)	4.30(9)
$\log g_2(\text{cgs})$	4.58(20)	4.18(15)	4.49(29)	4.26(8)
$a(R_\odot)$	1.92(17)	2.12(16)	2.24(30)	2.58(9)
$\log J_0(\text{cgs})$	51.50(19)	51.11(18)	51.72(33)	51.58(9)
$V_{max}(\text{mag})$	15.93(10)	15.51(11)	16.48(7)	10.11(8)
$AV(\text{mag})$	0.026(1)	0.037(1)	0.109(1)	0.029(1)
BC_1	-0.219(13)	-0.026(3)	-0.532(24)	-0.081(5)
BC_2	-0.273(15)	-0.023(3)	-0.641(26)	-0.109(7)

7. DISCUSSION AND CONCLUSION

We present the first comprehensive analyses of light curves and estimations of the absolute parameters for four contact binary star systems. Ground-based observations were conducted at two observatories located in the Northern and Southern Hemispheres, utilizing multiband CCD photometric filters. Time-series photometric data from TESS were only available for the DM Cir system. We modeled and analyzed the orbital period variations and light curves using the PHOEBE Python code. An acceptable fit to the observations is reached under the cool-spot assumption, implying that a cool spot on the secondary component is needed to explain the asymmetry in the maxima. We estimated the absolute physical parameters of the four systems using the Gaia DR3 parallax method. From the overall investigations, we drew the following conclusions:

- We extracted the times of minima from our observations and supplemented them with minima from the different literature. We updated the ephemeris for the L10772300, L11150338, L20372537, and DM Cir systems. The observational time span for these systems is approximately 8, 9, 10, and 4 years, respectively. Due to the short observational time span between the earliest and latest observed minima, as well as the limited number of available minima in the O-C diagrams, a linear least-squares fit was considered as the best representation of the data.
- The light curve solutions indicate that the effective-temperature differences between the components of systems are small, with the lowest value of 30 K for L11150338 and the highest of 149 K for L20372537. This result suggests that the temperature differences between the components of the target systems are consistent with the range of contact binaries (Poro et al. 2025e). The effective-temperature difference, defined as $\Delta T = |T_1 - T_2|$, quantifies the thermal disequilibrium between the two stellar components. In contact binary systems, both stars fill their Roche lobes and are enclosed within a common convective envelope, sharing a single equipotential surface. This configuration allows for continuous energy exchange through the common envelope, leading to thermal equilibrium between the components. From another point of view, according to Webbink (2003), the nearly equal depths of primary and secondary eclipses, as well as the absence of pronounced color variations in W UMa-type light curves, suggest that the components must be nearly identical in effective temperature. Detailed light curve synthesis models employing Roche geometry further confirm that the components of such binaries exist in a state of physical contact (Webbink 2003). The near-uniformity of effective temperature over the surface of a W UMa binary arises naturally from hydrostatic equilibrium within the common envelope, and that energy exchange between contact components is thus implicitly

demanded by hydrostatic equilibrium. This interpretation is consistent with the theoretical framework proposed by Lucy (1968a), in which the continuity of entropy within the common envelope enforces nearly equal fluxes from both stars. Consequently, the observed near equality of the component temperatures in our systems reflects energy transfer and thermal contact. Moreover, such near-equal effective temperatures are consistent with the behavior of most W UMa-type binaries reported in the literature, such as Poro et al. (2025d), where the majority of targets exhibit only small temperature differences between their components. The derived temperature difference of less than 400 K supports the interpretation that the components of our targets are in, or very close to, surface thermal equilibrium, while internal thermal equilibrium is not necessarily expected (Li et al. 2004; Yakut & Eggleton 2005; Fabry & Prša 2025b). The spectral classifications of the component stars were determined using the Cox (2015) and Eker et al. (2006) studies (Table 8).

- We employed the Gaia DR3 parallax method to estimate the absolute parameters of each system. This method is well-suited for this purpose, providing geometrically determined distances with substantially reduced systematic errors. The zero-point calibration by Lindegren et al. (2021), based on quasars, Large Magellanic Cloud stars, and physical binaries, guarantees consistent and precise measurements. However, this approach is reliable when the A_V value is low (Poro et al. 2024a). Our target systems align with this circumstance, as shown in Table 7. In the Gaia DR3 parallax approach, the total orbital semi-major axis is independently inferred from the properties of each component, yielding two determinations, a_1 and a_2 . In a physically consistent solution, these values are expected to agree; therefore, their difference, $\Delta a = |a_1 - a_2|$, is used as an internal consistency check between the astrometric parallax, orbital geometry, and the derived mass ratio (Hilditch 2001; Poro et al. 2024c). A $\Delta a < 0.1$ indicates acceptable consistency and serves as an additional proof of the reliability of the light curve solutions (Poro et al. 2024b). As presented in Table 8, the Δa values obtained for the targets are less than 0.1. Additionally, based on the effective temperature and mass of each component, it was determined that L10772300 and L11150338 are W-subtype, while the others are A-subtype.

- To investigate the evolutionary status of the four target systems, we constructed the mass–luminosity ($M - L$) and mass–radius ($M - R$) diagrams using the derived absolute parameters (Figure 6). The theoretical Zero-Age Main Sequence (ZAMS) and Terminal-Age Main Sequence (TAMS) relations were taken from Hurley et al. (2002) and are plotted as solid and dashed black lines, respectively. As shown in Figure 6, the $M - L$ and $M - R$ diagrams indicate that more mass stars are generally positioned closer to the ZAMS, while lower-mass components tend to lie near the TAMS. However, there is one exceptional target in this study; the lower-mass component of L11150338 lies away from the TAMS. This behavior is consistent with the long-standing interpretation that contact binaries, as interacting systems, cannot in general satisfy single-star mass-radius relations. As pointed out by Kuiper (1941), such relations are only expected to hold in the limiting case of equal-mass components, while systems with unequal masses necessarily deviate from single-star expectations. Subsequent studies have shown that binary interaction phases modify the internal structure of the components, altering the envelope-to-core mass ratio and, consequently, their mass-radius relations (Yakut & Eggleton 2005; Stepien 2005). In such systems, the less massive component is typically a more evolved star with a lower central hydrogen content and an expanded radius, while the more massive component lies close to the main sequence. If the less massive component were to evolve significantly beyond the main sequence, the system would likely merge on a thermal timescale (Poro et al. 2026a). This structure results from angular-momentum loss–driven evolution and past mass exchange leading to a mass-ratio reversal. Therefore, any direct comparison with the ZAMS and TAMS lines for single stars should be made with caution. Following the analysis of Poro et al. (2024d), the temperature-mass ($T_h - M_m$) relationship for contact binary systems is presented in Figure 6, where a linear relation (Equation 5) is fitted to the data. Here M_m denotes the mass of the more massive component.

$$\log M_m = (1.6185 \pm 0.0150) \times (\log T_h) + (-6.0186 \pm 0.0562). \quad (5)$$

The positions of the higher-mass, hotter components of each target system on the $T_h - M_m$ diagram align with the distribution of contact binaries. These components lie within the typical region of contact binary systems. We estimated the orbital angular momentum for each system (Table 7), and their locations are shown on the $J_0 - \log M_{tot}$ diagram (Figure 6). We utilized the parabolic line from the study by Eker et al. (2006), which shows that our targets are located below this curve, within the domain typically associated with contact binaries.

Based on the results of this study, we computed the ratio of spin to orbital angular momentum ($J_{\text{spin}}/J_{\text{orb}}$) for the targets using the classical relation

$$\frac{J_{\text{spin}}}{J_{\text{orb}}} = \frac{1+q}{q} \left[(k_1 r_1)^2 + (k_2 r_2)^2 q \right], \quad (6)$$

where q is the mass ratio, r_1 and r_2 are the fractional radii of the primary and secondary, and k_1 and k_2 are the respective gyration radii, with adopted values $k_1 = k_2 = 0.06$ from [Li & Zhang \(2006\)](#). We find that L10772300 has $J_{\text{spin}}/J_{\text{orb}} = 0.062(4)$, L11150338 has $0.190(4)$, L20372537 has $0.040(6)$, and DM Cir has $0.056(4)$. All of these values are well below the Darwin stability threshold ($J_{\text{spin}}/J_{\text{orb}} \sim 0.333$; [Hut 1980](#)), confirming that the systems are dynamically stable.

- In order to investigate the formation and evolution of W UMa-type contact binaries, [Yıldız & Doğan \(2013\)](#) proposes a method based on the observational properties of overluminous secondary components. In their method, if the central physical condition of the system's secondary component is similar to a single star of mass $M_L \approx L^{0.25}$ (in solar units), the initial mass of the secondary component can be estimated from the following equation:

$$M_{2i} = M_2 + \Delta M = M_2 + 2.50 (M_L - M_2 - 0.07)^{0.64}, \quad (7)$$

where M_2 represents the current mass of the secondary, and M_L is the luminosity-based mass estimated using equation 8.

$$M_L = \left(\frac{L_2}{1.49} \right)^{\frac{1}{4.216}}. \quad (8)$$

The initial mass of the primary component was estimated using equation 9. In this approach, the mass lost from the system is expressed as $M_{\text{lost}} = \gamma \Delta M$, where we adopted $\gamma = 0.664$ following the prescription of [Yıldız & Doğan \(2013\)](#). We emphasize that the degree of conservativeness of mass transfer depends on the evolutionary state of the mass-donor star. In particular, the value of γ derived by [Yıldız & Doğan \(2013\)](#) is based on the assumption that the initial mass transfer occurs when the donor is close to the TAMS. This assumption may not be strictly valid for long-lived contact binaries, which are expected to experience mass transfer during the main-sequence phase. Therefore, the initial mass estimates presented here should be regarded as model-dependent and subject to these underlying assumptions

$$M_{1i} = M_1 - (\Delta M - M_{\text{lost}}) = M_1 - \Delta M(1 - \gamma). \quad (9)$$

The formation and evolution of W UMa-type contact binaries are driven by nuclear and angular momentum evolution via magnetic braking ([Mestel 1968](#)), which causes the stars to fill their Roche lobes and exchange mass ([Okamoto & Sato 1970; Vilhu 1982](#)). The initially more massive component transfers material to its companion, leading to a mass ratio reversal. This process explains the systems' nearly identical temperatures and the overluminosity of the secondary ([Webbink 2003; Li et al. 2008](#)), a remnant of its higher initial mass and the energy transfer between components within the shared envelope.

According to the evolutionary framework of [Tutukov et al. \(2004\)](#), systems with M_{1i} between 0.2 and $1.5 M_{\odot}$ are expected to experience angular momentum loss. This process leads to orbital contraction and can ultimately result in contact between the components. As shown in Table 8, our systems fall within this mass range. However, the efficiency of magnetic braking is known to decrease for higher-mass primaries and becomes significantly reduced for $M_{1i} \gtrsim 1.3 M_{\odot}$ (e.g. [Pylyser & Savonije 1988; Podsiadlowski et al. 2002](#)). Therefore, the evolution of our systems is most likely governed by magnetic braking, which drives the loss of orbital angular momentum and promotes their evolution toward contact configurations. The values of M_{2i} in our target systems are higher than their current masses (see Table 8), suggesting that the secondary components of these contact binaries have internal structures that might differ from those of normal main-sequence stars ([Yıldız & Doğan 2013](#)).

The difference between the current secondary masses and the inferred initial values M_{2i} reflects the assumptions adopted in our evolutionary framework, particularly the non-conservative mass transfer prescription with $\gamma = 0.664$ following [Yıldız & Doğan \(2013\)](#). Given the masses and orbital periods, target systems are most plausibly formed through AML, with the onset of interaction occurring during the main-sequence phase. In such systems, both AML and Roche-lobe overflow (RLOF) are expected to operate concurrently during their evolution toward contact configurations ([Hilditch et al. 1988; Eggleton 2012](#)). Compared to the other targets, the mass lost in L20372537 is lower and can be explained by its higher mass ratio relative to the other three systems.

- Energy is transferred from the hotter component to the cooler one through the common envelope and causes the two components to have nearly the same temperature even though their masses are quite different ([Lucy 1968a,b](#)). Building on this behavior, understanding the mechanisms and efficiency of energy transfer has been a longstanding focus of extensive studies. A significant step forward was provided by [Mochnacki \(1981\)](#), who showed the role of mass ratio in the relative energy transfer rate and normal mass-luminosity relation for independent stars. Subsequent studies,

such as [Wang \(1994\)](#), further expand this framework and demonstrate that the relative energy transfer rate increases continuously as the mass ratio increases, while [Liu & Yang \(2000\)](#) showed that it also depends on the evolutionary degree of the primary. In addition, [Csizmadia & Klagyivik \(2004\)](#) analyzed the properties of these systems using the large catalog of contact binaries to show that the energy transfer parameter can be expressed as a simple function of the mass and luminosity ratios.

Building on these foundations, [Jiang et al. \(2009\)](#) analyzed a sample of 133 W UMa-type contact binaries and examined how energy transfer impacts the secondary components. Based on the distribution of temperature differences, they showed that properties of the common envelope might not have a significant effect on energy transfer between the components of these systems. Under the assumptions of contact configurations with nearly uniform effective temperatures and ZAMS primaries, the relative energy transfer rates can be described using the formalism introduced by [Mochnacki \(1981\)](#)

$$U_1 = \frac{r^2 t^4 - q^\alpha}{1 + q^\alpha} \quad (10)$$

$$U_2 = \log\left[\frac{r^2 t^4 - q^\alpha}{q^\alpha(1 + r^2 t^4)}\right], \quad (11)$$

where $r = R_2/R_1$, $t = T_2/T_1$ correspond to radius and temperature ratios, and $\alpha = 3.42$ represents the exponent of the mass luminosity relation.

In order to investigate the overluminosity of secondaries and its connection to energy transfer between the components, the nuclear luminosity of each component can be approximated using the relation given by [Demircan & Kahraman \(1991\)](#)

$$L_0 \simeq 1.03 M^{3.42}, \quad 0.1 \leq M \leq 120, \quad (12)$$

Equation (12) represents an approximate mass-luminosity relation for single main-sequence stars and should therefore be applied and interpreted with caution for contact binary components.

As shown in Figure 7, [Jiang et al. \(2009\)](#) derived the theoretical luminosity relation in which $\log(L_1 + L_2) = \log(L_{10} + L_{20})$, along with theoretical fits for the distribution of U_1 and U_2 as a function of q , as well as $\log(R_2/R_1)$ versus $\log q$, expressed as

$$U_1 = \frac{q^{0.92} - q^{3.42}}{1 + q^{3.42}}, \quad (13)$$

$$U_2 = \log\left[\frac{q^{0.92} - q^{3.42}}{q^{3.42}(1 + q^{0.92})}\right]. \quad (14)$$

$$\log(R_2/R_1) = (0.431 \pm 0.006) \log q - (0.007 \pm 0.003). \quad (15)$$

Equation 13 closely reproduces the results of [Fabry et al. \(2023\)](#) for the fillout factor when the Roche-lobe areas of the secondary and primary stars, S_2 and S_1 , are approximated to be proportional to their masses, that is, $S_2/S_1 \simeq q$. Relation 15 is consistent with the classical Roche-lobe geometry and the well-established relations originally described by [KOPAL \(1959\)](#).

To extend the applicability of this theoretical framework, we have collected the physical parameters of 407 W UMa-type binaries from the study by [Poro et al. \(2025a\)](#), along with the four target systems analyzed in this study. Although the catalog in that study contains 818 systems, we restricted our sample to those that are consistent with the assumptions provided by [Jiang et al. \(2009\)](#). We considered only systems in which both components fill their inner Roche lobes ($R_2/R_1 = q^{0.46}$), and have a $\Delta T_{eff} < 400K$. In addition, the primaries were required to be consistent with zero-age main sequence stars. It is also important to note that systems lacking any of the required parameters are excluded from the sample, as these values are essential for our analysis. Using this selective dataset, we calculated the energy transfer rate of the primary (U_1) and secondary (U_2) components for a wide range of mass ratios and estimated the nuclear luminosity for each component. Figure 7 shows the full sample of 411 targets, Table 9 lists the results for the four systems analyzed in detail, and statistical fits (with uncertainties) were performed for each panel using equations 16–19.

Table 8. Some conclusions regarding to the evolutionary history of the four target systems.

Systems	$ \Delta T $ (K)	$ \Delta a $	Sp. cat.	Subtype	$M_{1i}(M_{\odot})$	$M_{2i}(M_{\odot})$	$M_{lost}(M_{\odot})$
L10772300	143	0.03	K0-K1	W	0.942(331)	1.168(241)	0.510(231)
L11150338	30	0.08	F8-F8	W	0.625(271)	1.733(52)	1.058(49)
L20372537	149	0.01	K3-K2	A	1.016(188)	0.921(69)	0.127(11)
DM Cir	148	0.01	G5-G6	A	0.712(127)	1.595(80)	0.767(85)

First, the relation between $\log(L_1 + L_2)$ and $\log(L_{10} + L_{20})$ for both A- and W-subtype binaries is well described by a statistical linear fit.

$$\log(L_1 + L_2) = (0.747 \pm 0.083) \log(L_{10} + L_{20}) + (0.104 \pm 0.047). \quad (16)$$

The best fit for the relative energy transfer rates versus the mass ratio is represented by a second-degree polynomial and a third-degree polynomial, given by

$$U_1 = (-1.624 \pm 0.149) q^2 + (1.567 \pm 0.139) q - (0.006 \pm 0.027). \quad (17)$$

$$U_2 = (-11.368 \pm 1.276) q^3 + (18.814 \pm 1.780) q^2 - (12.914 \pm 0.713) q + (3.632 \pm 0.080). \quad (18)$$

The relation between $\log(R_2/R_1)$ and $\log(q)$ is well described by a logarithmic fit.

$$\log\left(\frac{R_2}{R_1}\right) = (0.419 \pm 0.007) \log(q) - (0.008 \pm 0.004). \quad (19)$$

As shown in Figure 7, the 411 systems align well with the theoretical relations derived by [Jiang et al. \(2009\)](#) in all four panels.

L10772300 located below both the statistical fit and the theoretical luminosity relation in panel (a), exhibiting a deviation of $|\Delta \log L| > 0.4$. Such deviations often indicate evolved components, particularly in low-mass W UMa binaries, which exhibit higher velocity dispersions and older mean kinematic ages ([Bilir et al. 2005](#)). Alternatively, they may arise from the presence of a third component whose light contribution biases the light curve solution and shifts the inferred luminosities ([Pribulla & Rucinski 2006](#)).

In panel (b), L10772300 is near the peak of the $U_1(q)$ curve, indicating that the primary must transfer the maximum energy to bring the secondary to the same temperature. In panel (c), its U_2 value confirms that the secondary is overluminous, the expected consequence of strong thermal coupling in contact binaries ([Webbink 2003](#)). We emphasize that, in our sample, the secondary is defined as the less massive component, regardless of its temperature, following the convention that the primary is always the more massive star in contact binaries.

L11150338 expresses strong energy transfer, distinguishing it from the other target systems. In panel (a), it is above the statistical and theoretical lines, indicating that its observed luminosity exceeds its nuclear luminosity, suggesting thermal redistribution. L11150338 has a low mass ratio, corresponding to a low U_1 . Panel (c) shows that L11150338 exhibits the largest U_2 value among the four targets, indicating that its secondary is strongly overluminous relative to its nuclear luminosity, which is expected due to its relatively high mass ratio.

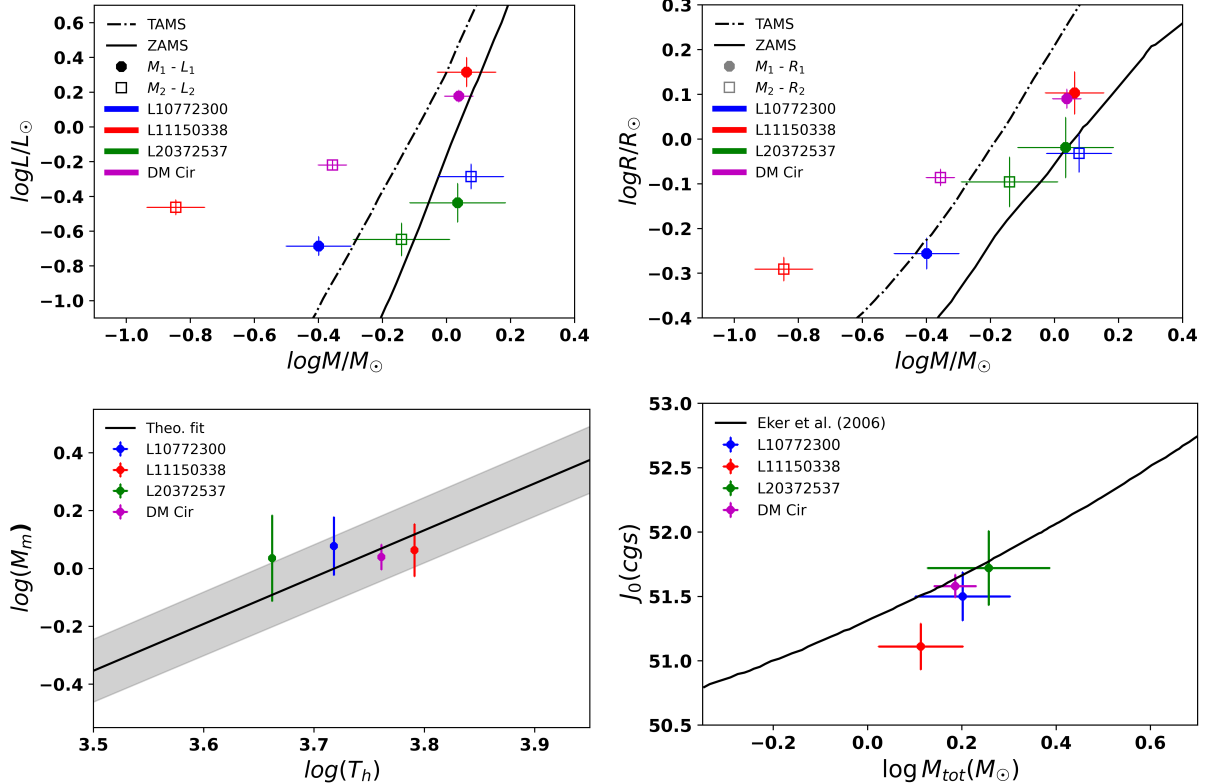
L20372537 is located below both the statistical and the theoretical luminosity relation in panel (a), again showing a deviation of $|\Delta \log L| > 0.4$. In panel (b), the mass ratio of L20372537 ($q = 0.669$) places it in the descending part of $U_1(q)$, where the primary needs to transfer relatively less energy due to the comparable mass of the secondary. Its deviation from the curves is consistent with [Jiang et al. \(2009\)](#), which found that systems with larger unequal component temperatures display more deviation from the expected energy transfer curve. The value of U_2 for L20372537 is -0.058 , indicating minimal luminosity enhancement of the secondary component.

DM Cir agrees well with both theoretical and statistical relations in all four panels, following the expectations for efficient energy transfer given the component radii, luminosities, and masses. Its position in parameter space suggests structural and thermal properties consistent with those expected for moderate mass ratio systems in stable contact.

Finally, all four target systems align closely with the theoretical relation from equation (8) of [Jiang et al. \(2009\)](#) in panel (d), indicating that their geometry is consistent with a Roche filling configuration.

Table 9. Relative energy transfer rates and nuclear luminosities for the components of the four target systems.

Systems	L_{10}	L_{20}	$U_{1,rtq}$	$U_{2,rtq}$
L10772300	1.921(1698)	0.045(42)	0.373(110)	1.063(485)
L11150338	1.711(1362)	0.001(1)	0.163(44)	2.249(102)
L20372537	1.340(1867)	0.351(493)	0.284(224)	-0.058(362)
DM Cir	1.427(532)	0.062(24)	0.340(55)	0.755(94)

**Figure 6.** $M-L$, $M-R$, T_h-M_m , and $M_{\text{tot}}-J_0$ relation diagrams for the studied contact binaries.

DATA AVAILABILITY

The ground-based observations are provided in the online supplementary materials of this paper.

ACKNOWLEDGMENTS

We sincerely thank the referee for their constructive comments and valuable suggestions, which significantly improved the quality and clarity of this manuscript. This manuscript, including the observation, analysis, and writing processes, was provided by the BSN project (<https://bsnp.info>). Ground-based observations (LINEAR 10772300, LINEAR 11150338, and LINEAR 20372537 systems) were conducted with the cooperation of the Observatorio Astronómico Nacional on the Sierra San Pedro Mártir (OAN-SPM), Baja California, México. We used IRAF, distributed by the National Optical Observatories and operated by the Association of Universities for Research in Astronomy, Inc., under a cooperative agreement with the National Science Foundation. We used results reported by the European Space Agency mission Gaia(<http://www.cosmos.esa.int/gaia>). In this work, we utilize observations obtained by the TESS mission, supported through NASA's Explorer Program.

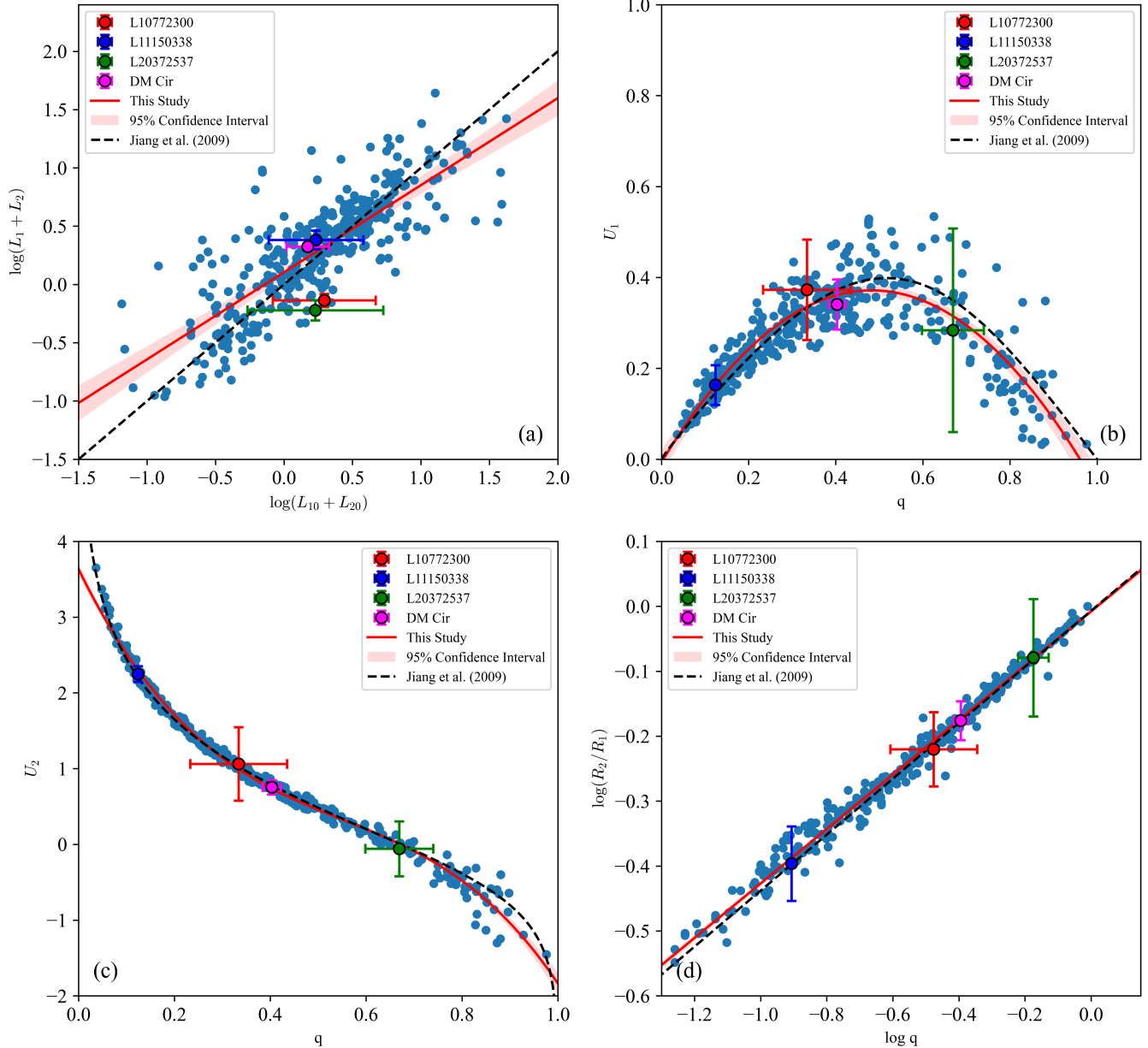


Figure 7. Distributions of $\log(L_1 + L_2)$ versus $\log(L_{10} + L_{20})$, U_1 , U_2 , and $\log(R_2/R_1)$ as functions of mass ratio for 411 W UMa systems (blue dots) and the solid lines represent the statistical fits.

APPENDIX

The appendix provides the measured primary and secondary eclipse timings for the four analyzed contact binary systems, obtained from TESS photometric observations.

Table A1. Times of Minima extracted from the TESS data for DM Cir. The minimums have been reduced from 2,400,000.

Min.(BJD)	Error	Epoch	O-C	Min.(BJD)	Error	Epoch	O-C	Min.	Error	Epoch	O-C
59333.8952	0.0002	16345.5	-0.0200	59346.2723	0.0001	16377.5	-0.0197	59359.8097	0.0002	16412.5	-0.0196
59334.0885	0.0002	16346	-0.0201	59347.4328	0.0002	16380.5	-0.0196	59360.0023	0.0002	16413	-0.0203
59334.2818	0.0002	16346.5	-0.0202	59347.6253	0.0002	16381	-0.0205	59360.1965	0.0002	16413.5	-0.0195
59334.4751	0.0002	16347	-0.0203	59347.8196	0.0002	16381.5	-0.0196	59360.3892	0.0002	16414	-0.0203
59334.6686	0.0002	16347.5	-0.0201	59348.0122	0.0002	16382	-0.0204	59361.9359	0.0002	16418	-0.0206
59334.8618	0.0001	16348	-0.0204	59348.2064	0.0002	16382.5	-0.0196	59362.1305	0.0002	16418.5	-0.0194
59335.0554	0.0002	16348.5	-0.0201	59348.3989	0.0002	16383	-0.0204	59362.3227	0.0002	16419	-0.0206
59335.2486	0.0002	16349	-0.0204	59348.5931	0.0002	16383.5	-0.0196	59362.5173	0.0002	16419.5	-0.0194
59335.4423	0.0002	16349.5	-0.0200	59348.7857	0.0001	16384	-0.0205	59362.7095	0.0002	16420	-0.0206
59335.6353	0.0002	16350	-0.0204	59348.9799	0.0002	16384.5	-0.0196	59362.9041	0.0002	16420.5	-0.0194
59335.8290	0.0002	16350.5	-0.0200	59349.1724	0.0002	16385	-0.0205	59363.0962	0.0002	16421	-0.0206
59336.0221	0.0001	16351	-0.0204	59349.3668	0.0002	16385.5	-0.0195	59363.2910	0.0002	16421.5	-0.0192
59336.2158	0.0001	16351.5	-0.0201	59349.5591	0.0002	16386	-0.0206	59363.4830	0.0002	16422	-0.0206
59336.4089	0.0002	16352	-0.0204	59349.7535	0.0002	16386.5	-0.0196	59363.6778	0.0002	16422.5	-0.0192
59336.6026	0.0002	16352.5	-0.0200	59349.9459	0.0001	16387	-0.0206	59363.8698	0.0002	16423	-0.0206
59336.7957	0.0002	16353	-0.0204	59350.1403	0.0002	16387.5	-0.0196	59364.0647	0.0002	16423.5	-0.0191
59336.9895	0.0002	16353.5	-0.0200	59350.3327	0.0002	16388	-0.0205	59364.2566	0.0002	16424	-0.0206
59337.1824	0.0002	16354	-0.0204	59350.5271	0.0002	16388.5	-0.0195	59364.4515	0.0002	16424.5	-0.0191
59337.3764	0.0002	16354.5	-0.0198	59350.7195	0.0002	16389	-0.0205	59364.6433	0.0002	16425	-0.0207
59337.5691	0.0002	16355	-0.0205	59350.9138	0.0002	16389.5	-0.0196	59364.8382	0.0002	16425.5	-0.0192
59337.7632	0.0002	16355.5	-0.0198	59351.1063	0.0002	16390	-0.0205	59365.0301	0.0002	16426	-0.0207
59337.9559	0.0002	16356	-0.0205	59351.3006	0.0002	16390.5	-0.0196	59365.2249	0.0002	16426.5	-0.0192
59338.1502	0.0002	16356.5	-0.0196	59351.4931	0.0002	16391	-0.0205	59365.4169	0.0002	16427	-0.0207
59338.3425	0.0002	16357	-0.0206	59351.6874	0.0002	16391.5	-0.0196	59365.6117	0.0002	16427.5	-0.0193
59338.5370	0.0002	16357.5	-0.0196	59351.8799	0.0002	16392	-0.0204	59365.8036	0.0002	16428	-0.0207
59338.7293	0.0002	16358	-0.0206	59352.0742	0.0002	16392.5	-0.0195	59365.9985	0.0002	16428.5	-0.0192
59338.9238	0.0002	16358.5	-0.0195	59352.2668	0.0002	16393	-0.0203	59366.1903	0.0002	16429	-0.0208
59339.1161	0.0002	16359	-0.0206	59352.4609	0.0001	16393.5	-0.0196	59366.3853	0.0002	16429.5	-0.0192
59339.3106	0.0002	16359.5	-0.0194	59352.6535	0.0001	16394	-0.0204	59366.5771	0.0002	16430	-0.0208
59339.5029	0.0002	16360	-0.0205	59352.8477	0.0002	16394.5	-0.0196	59366.7720	0.0002	16430.5	-0.0192
59339.6974	0.0002	16360.5	-0.0195	59353.0404	0.0001	16395	-0.0203	59366.9638	0.0002	16431	-0.0208
59339.8898	0.0001	16361	-0.0205	59353.2346	0.0002	16395.5	-0.0195	59367.1590	0.0002	16431.5	-0.0191
59340.0840	0.0002	16361.5	-0.0196	59353.4272	0.0002	16396	-0.0202	59367.3504	0.0002	16432	-0.0210
59340.2767	0.0002	16362	-0.0204	59353.6213	0.0002	16396.5	-0.0195	59367.5458	0.0002	16432.5	-0.0190
59340.4707	0.0002	16362.5	-0.0197	59353.8142	0.0002	16397	-0.0200	59367.7373	0.0002	16433	-0.0209
59340.6636	0.0002	16363	-0.0202	59354.0081	0.0002	16397.5	-0.0195	59367.9325	0.0002	16433.5	-0.0191
59340.8575	0.0002	16363.5	-0.0197	59354.2007	0.0001	16398	-0.0202	59368.1240	0.0002	16434	-0.0210
59341.0503	0.0001	16364	-0.0203	59354.3949	0.0002	16398.5	-0.0195	59368.5108	0.0002	16435	-0.0210
59341.2443	0.0002	16364.5	-0.0197	59354.5876	0.0002	16399	-0.0202	59368.7061	0.0002	16435.5	-0.0190
59341.4370	0.0002	16365	-0.0203	59354.7816	0.0002	16399.5	-0.0195	59368.8976	0.0003	16436	-0.0209
59341.6310	0.0002	16365.5	-0.0197	59354.9744	0.0001	16400	-0.0202	59369.0929	0.0002	16436.5	-0.0190
59341.8238	0.0002	16366	-0.0204	59355.1683	0.0002	16400.5	-0.0196	59369.2844	0.0002	16437	-0.0209
59342.0177	0.0002	16366.5	-0.0198	59355.3611	0.0001	16401	-0.0202	59369.4797	0.0002	16437.5	-0.0190
59342.2105	0.0002	16367	-0.0204	59355.5551	0.0002	16401.5	-0.0196	59369.6712	0.0002	16438	-0.0209
59342.4045	0.0002	16367.5	-0.0198	59355.7480	0.0002	16402	-0.0202	59369.8666	0.0002	16438.5	-0.0189
59342.5972	0.0002	16368	-0.0205	59355.9419	0.0002	16402.5	-0.0196	59370.0580	0.0003	16439	-0.0209
59342.7912	0.0002	16368.5	-0.0199	59356.1347	0.0002	16403	-0.0202	59370.2534	0.0002	16439.5	-0.0189
59342.9840	0.0002	16369	-0.0205	59356.3286	0.0002	16403.5	-0.0197	59370.4448	0.0002	16440	-0.0208
59343.1780	0.0002	16369.5	-0.0198	59356.5215	0.0001	16404	-0.0202	59370.6401	0.0002	16440.5	-0.0189
59343.3707	0.0002	16370	-0.0205	59356.7154	0.0002	16404.5	-0.0197	59370.8317	0.0002	16441	-0.0207
59343.5648	0.0001	16370.5	-0.0198	59356.9082	0.0002	16405	-0.0202	59371.0270	0.0002	16441.5	-0.0188
59343.7574	0.0001	16371	-0.0206	59357.1022	0.0002	16405.5	-0.0197	59371.2185	0.0002	16442	-0.0207
59343.9517	0.0002	16371.5	-0.0198	59357.2950	0.0002	16406	-0.0202	59371.4137	0.0002	16442.5	-0.0189
59344.1442	0.0002	16372	-0.0206	59357.4889	0.0002	16406.5	-0.0197	59371.6053	0.0002	16443	-0.0206
59344.3384	0.0002	16372.5	-0.0197	59357.6818	0.0001	16407	-0.0202	59371.8004	0.0002	16443.5	-0.0190
59344.5309	0.0002	16373	-0.0206	59357.8757	0.0002	16407.5	-0.0197	59371.9921	0.0002	16444	-0.0207
59344.7252	0.0002	16373.5	-0.0197	59358.0686	0.0001	16408	-0.0202	59372.1872	0.0003	16444.5	-0.0189
59344.9178	0.0002	16374	-0.0206	59358.2625	0.0002	16408.5	-0.0197	59372.3788	0.0002	16445	-0.0207
59345.1119	0.0002	16374.5	-0.0198	59358.4552	0.0002	16409	-0.0203	59372.5739	0.0002	16445.5	-0.0190
59345.3046	0.0002	16375	-0.0206	59358.6493	0.0002	16409.5	-0.0197	59372.7656	0.0002	16446	-0.0207
59345.4987	0.0002	16375.5	-0.0198	59358.8420	0.0001	16410	-0.0203	59372.9607	0.0002	16446.5	-0.0190
59345.6914	0.0002	16376	-0.0205	59359.2287	0.0001	16411	-0.0204	59373.1524	0.0002	16447	-0.0206
59345.8855	0.0002	16376.5	-0.0198	59359.4229	0.0002	16411.5	-0.0196	59373.5392	0.0002	16448	-0.0207
59346.0782	0.0002	16377	-0.0204	59359.6155	0.0002	16412	-0.0204	59373.7342	0.0002	16448.5	-0.0190

Table A1. Continued.

Min.(BJD)	Error	Epoch	O-C	Min.	Error	Epoch	O-C	Min.(BJD)	Error	Epoch	O-C
59373.9259	0.0002	16449	-0.0207	59388.8182	0.0002	16487.5	-0.0194	60081.3371	0.0002	18278	-0.0247
59374.1210	0.0002	16449.5	-0.0190	59389.0098	0.0003	16488	-0.0211	60081.7238	0.0002	18279	-0.0248
59374.3127	0.0002	16450	-0.0207	59389.2048	0.0002	16488.5	-0.0195	60081.9200	0.0001	18279.5	-0.0219
59374.5077	0.0002	16450.5	-0.0191	59389.3966	0.0003	16489	-0.0211	60082.1106	0.0002	18280	-0.0247
59374.6990	0.0003	16451	-0.0212	59389.5922	0.0002	16489.5	-0.0189	60082.3068	0.0001	18280.5	-0.0219
59376.0547	0.0002	16454.5	-0.0192	60068.7693	0.0002	18245.5	-0.0222	60082.4974	0.0002	18281	-0.0247
59376.2464	0.0002	16455	-0.0209	60068.9606	0.0002	18246	-0.0243	60082.8841	0.0002	18282	-0.0248
59376.6333	0.0002	16456	-0.0208	60069.1565	0.0001	18246.5	-0.0218	60083.0804	0.0002	18282.5	-0.0218
59376.8282	0.0002	16456.5	-0.0192	60069.3474	0.0002	18247	-0.0243	60083.2708	0.0002	18283	-0.0249
59377.0200	0.0002	16457	-0.0208	60069.5432	0.0001	18247.5	-0.0218	60083.8540	0.0001	18284.5	-0.0218
59377.4068	0.0002	16458	-0.0208	60069.7341	0.0002	18248	-0.0243	60084.0444	0.0002	18285	-0.0248
59377.6019	0.0002	16458.5	-0.0191	60069.9300	0.0001	18248.5	-0.0219	60084.2407	0.0001	18285.5	-0.0218
59377.7936	0.0002	16459	-0.0208	60070.1209	0.0002	18249	-0.0243	60084.4311	0.0002	18286	-0.0248
59377.9886	0.0002	16459.5	-0.0192	60070.3167	0.0001	18249.5	-0.0219	60084.6275	0.0001	18286.5	-0.0219
59378.1804	0.0002	16460	-0.0207	60070.5077	0.0002	18250	-0.0243	60084.8179	0.0002	18287	-0.0249
59378.5672	0.0002	16461	-0.0208	60070.7035	0.0001	18250.5	-0.0219	60085.0143	0.0001	18287.5	-0.0218
59378.7622	0.0002	16461.5	-0.0191	60070.8945	0.0002	18251	-0.0243	60085.2047	0.0002	18288	-0.0248
59378.9539	0.0002	16462	-0.0208	60071.0902	0.0001	18251.5	-0.0219	60085.4012	0.0001	18288.5	-0.0217
59379.1489	0.0002	16462.5	-0.0192	60071.2812	0.0002	18252	-0.0243	60085.5915	0.0002	18289	-0.0248
59379.3408	0.0002	16463	-0.0207	60071.4769	0.0001	18252.5	-0.0220	60085.7880	0.0002	18289.5	-0.0217
59379.5356	0.0002	16463.5	-0.0193	60071.6680	0.0002	18253	-0.0243	60085.9783	0.0002	18290	-0.0248
59379.7274	0.0002	16464	-0.0209	60071.8637	0.0001	18253.5	-0.0220	60086.1747	0.0002	18290.5	-0.0217
59379.9224	0.0002	16464.5	-0.0192	60072.0548	0.0002	18254	-0.0243	60086.3651	0.0002	18291	-0.0248
59380.1141	0.0002	16465	-0.0210	60072.2505	0.0001	18254.5	-0.0220	60086.7518	0.0002	18292	-0.0248
59380.3092	0.0002	16465.5	-0.0192	60072.4416	0.0002	18255	-0.0243	60086.9483	0.0001	18292.5	-0.0218
59380.5008	0.0002	16466	-0.0210	60072.6373	0.0001	18255.5	-0.0220	60087.1387	0.0002	18293	-0.0247
59380.6961	0.0002	16466.5	-0.0192	60072.8283	0.0002	18256	-0.0244	60087.3350	0.0002	18293.5	-0.0218
59380.8875	0.0002	16467	-0.0211	60073.0241	0.0001	18256.5	-0.0219	60087.5254	0.0002	18294	-0.0248
59381.0828	0.0003	16467.5	-0.0192	60073.2150	0.0002	18257	-0.0244	60087.7218	0.0001	18294.5	-0.0218
59381.2742	0.0003	16468	-0.0211	60073.4108	0.0001	18257.5	-0.0221	60087.9121	0.0002	18295	-0.0248
59381.4696	0.0002	16468.5	-0.0192	60073.6018	0.0002	18258	-0.0244	60088.1085	0.0001	18295.5	-0.0219
59381.6611	0.0003	16469	-0.0211	60073.7976	0.0001	18258.5	-0.0220	60088.2988	0.0002	18296	-0.0249
59381.8564	0.0002	16469.5	-0.0191	60073.9886	0.0002	18259	-0.0244	60088.6856	0.0002	18297	-0.0249
59382.0478	0.0003	16470	-0.0212	60074.1843	0.0001	18259.5	-0.0221	60088.8820	0.0001	18297.5	-0.0219
59382.2433	0.0002	16470.5	-0.0190	60074.3753	0.0002	18260	-0.0244	60089.0724	0.0002	18298	-0.0249
59382.4344	0.0003	16471	-0.0213	60074.5710	0.0001	18260.5	-0.0221	60089.2687	0.0001	18298.5	-0.0219
59382.6299	0.0003	16471.5	-0.0192	60074.7622	0.0002	18261	-0.0244	60089.4591	0.0002	18299	-0.0250
59382.8218	0.0002	16472	-0.0207	60074.9577	0.0001	18261.5	-0.0222	60089.6556	0.0002	18299.5	-0.0219
59383.0167	0.0002	16472.5	-0.0192	60075.1490	0.0002	18262	-0.0243	60089.8459	0.0002	18300	-0.0250
59383.2081	0.0002	16473	-0.0212	60075.3445	0.0001	18262.5	-0.0222	60090.0422	0.0001	18300.5	-0.0220
59383.5949	0.0003	16474	-0.0212	60075.5357	0.0002	18263	-0.0244	60090.2334	0.0001	18301	-0.0242
59383.7903	0.0003	16474.5	-0.0191	60075.7313	0.0001	18263.5	-0.0222	60090.6195	0.0002	18302	-0.0249
59383.9816	0.0003	16475	-0.0212	60075.9226	0.0001	18264	-0.0242	60091.0062	0.0002	18303	-0.0250
59384.3684	0.0002	16476	-0.0212	60076.3091	0.0002	18265	-0.0245	60091.2026	0.0001	18303.5	-0.0220
59384.5636	0.0002	16476.5	-0.0193	60076.5049	0.0001	18265.5	-0.0221	60091.3930	0.0002	18304	-0.0250
59384.7552	0.0002	16477	-0.0212	60076.6959	0.0002	18266	-0.0245	60091.7797	0.0002	18305	-0.0250
59384.9504	0.0002	16477.5	-0.0194	60077.0827	0.0002	18267	-0.0245	60091.9762	0.0002	18305.5	-0.0219
59385.1420	0.0003	16478	-0.0211	60077.2784	0.0001	18267.5	-0.0222	60092.1665	0.0002	18306	-0.0250
59385.5288	0.0003	16479	-0.0212	60077.4695	0.0002	18268	-0.0245	60092.3630	0.0002	18306.5	-0.0219
59385.7238	0.0002	16479.5	-0.0195	60077.6653	0.0001	18268.5	-0.0221	60092.5533	0.0002	18307	-0.0250
59385.9156	0.0002	16480	-0.0211	60077.8563	0.0002	18269	-0.0245	60092.7498	0.0002	18307.5	-0.0219
59386.1106	0.0002	16480.5	-0.0195	60078.2431	0.0002	18270	-0.0245	60092.9400	0.0002	18308	-0.0251
59386.3024	0.0003	16481	-0.0211	60078.6298	0.0002	18271	-0.0245	60093.3268	0.0002	18309	-0.0251
59386.4976	0.0002	16481.5	-0.0193	60078.8257	0.0001	18271.5	-0.0221	60093.5234	0.0002	18309.5	-0.0218
59386.6892	0.0003	16482	-0.0211	60079.0166	0.0002	18272	-0.0245	60093.7136	0.0002	18310	-0.0251
59387.0760	0.0003	16483	-0.0210	60079.2125	0.0001	18272.5	-0.0220	60093.9103	0.0002	18310.5	-0.0217
59387.2712	0.0002	16483.5	-0.0192	60079.4033	0.0002	18273	-0.0246	60094.1004	0.0002	18311	-0.0250
59387.4627	0.0003	16484	-0.0211	60079.7900	0.0002	18274	-0.0246	60094.4873	0.0002	18312	-0.0249
59387.6579	0.0003	16484.5	-0.0194	60079.9861	0.0001	18274.5	-0.0220	60094.6839	0.0002	18312.5	-0.0217
59387.8496	0.0003	16485	-0.0210	60080.1768	0.0002	18275	-0.0246	60094.8741	0.0002	18313	-0.0248
59388.0446	0.0002	16485.5	-0.0194	60080.5635	0.0002	18276	-0.0247	60095.2609	0.0002	18314	-0.0249
59388.2362	0.0003	16486	-0.0211	60080.7596	0.0001	18276.5	-0.0220	60095.4573	0.0002	18314.5	-0.0218
59388.4314	0.0002	16486.5	-0.0194	60080.9503	0.0002	18277	-0.0247	60095.6477	0.0002	18315	-0.0248
59388.6231	0.0002	16487	-0.0210	60081.1464	0.0001	18277.5	-0.0219	60096.0344	0.0002	18316	-0.0249

REFERENCES

Ahumada, R., Prieto, C. A., Almeida, A., et al. 2020, *ApJS*, 249, 3

Bellm, E. C., Kulkarni, S. R., Barlow, T., et al. 2019, *PASP*, 131, 068003

Bilir, S., Karataş, Y., Demircan, O., & Eker, Z. 2005, *MNRAS*, 357, 497

Binnendijk, L. 1970, *vistas in Astronomy*, 12, 217

Castelli, F., & Kurucz, R. L. 2004, arXiv preprint [astro-ph/0405087](https://arxiv.org/abs/astro-ph/0405087)

Conroy, K. E., Kochoska, A., Hey, D., et al. 2020, *ApJS*, 250, 34

Cox, A. N. 2015, *Allen's astrophysical quantities* (Springer)

Csizmadia, S., & Klagyivik, P. 2004, *Astronomy & Astrophysics*, 426, 1001

Demircan, O., & Kahraman, G. 1991, *Astrophysics and Space Science*, 181, 313

Drake, A., Graham, M., Djorgovski, S., et al. 2014, *ApJS*, 213, 9

Eastman, J., Siverd, R., & Gaudi, B. S. 2010, *PASP*, 122, 935

Eggleton, P. P. 2012, *Journal of Astronomy and Space Sciences*, 29, 145

Eker, Z., Demircan, O., Bilir, S., & Karataş, Y. 2006, *MNRAS*, 373, 1483

Fabry, M., Marchant, P., Langer, N., & Sana, H. 2023, *A&A*, 672, A175

Fabry, M., & Prša, A. 2025a, *ApJ*, 994, 7

—. 2025b, *ApJ*, 995, 19

Flower, P. J. 1996, *ApJv*. 469, p. 355, 469, 355

Gazeas, K., & Stępień, K. 2008, *Monthly Notices of the Royal Astronomical Society*, 390, 1577

Goodman, J., & Weare, J. 2010, *Communications in applied mathematics and computational science*, 5, 65

Green, G. M., Schlafly, E., Zucker, C., Speagle, J. S., & Finkbeiner, D. 2019, *ApJ*, 887, 93

Hilditch, R., King, D., & McFarlane, T. 1988, *MNRAS*(ISSN 0035-8711), vol. 231, March 15, 1988, p. 341-352., 231, 341

Hilditch, R. W. 2001, *An introduction to close binary stars* (Cambridge University Press)

Houk, N. 1975, Ann Arbor : Dept. of Astronomy, University of Michigan : distributed by University Microfilms International

Hurley, J. R., Tout, C. A., & Pols, O. R. 2002, *MNRAS*, 329, 897

Hut, P. 1980, *Astronomy and Astrophysics*, vol. 92, no. 1-2, Dec. 1980, p. 167-170., 92, 167

Jayasinghe, T., Kochanek, C., Stanek, K., et al. 2018, *MNRAS*, 477, 3145

Jayasinghe, T., Stanek, K., Kochanek, C., et al. 2019, *MNRAS*, 486, 1907

Jiang, D., Han, Z., Jiang, T., & Li, L. 2009, *MNRAS*, 396, 2176

Kallrath, J., Milone, E. F., & Wilson, R. 2009, *Eclipsing binary stars: modeling and analysis*, Vol. 11 (Springer)

Knote, M. F., Caballero-Nieves, S. M., Gokhale, V., Johnston, K. B., & Perlman, E. S. 2022, *ApJS*, 262, 10

KOPAL, Z. 1959, Chapman-Hall and John Wiley, London and New York, Sec. II, 5, 60

Kouzuma, S. 2019, *PASJ*, 71, 21

Kuiper, G. P. 1941, *Astrophysical Journal*, vol. 93, p. 133, 93, 133

Latham, D. W., Mazeh, T., Stefanik, R. P., et al. 1992, in *International Astronomical Union Colloquium*, Vol. 135, Cambridge University Press, 158–160

Latham, D. W., Stefanik, R. P., Torres, G., et al. 2002, *AJ*, 124, 1144

Li, L., Han, Z., & Zhang, F. 2004, arXiv preprint [astro-ph/0412072](https://arxiv.org/abs/astro-ph/0412072)

Li, L., & Zhang, F. 2006, *MNRAS*, 369, 2001

Li, L., Zhang, F., Han, Z., Jiang, D., & Jiang, T. 2008, *MNRAS*, 387, 97

Lindgren, L., Bastian, U., Biermann, M., et al. 2021, *A&A*, 649, A4

Liu, Q., & Yang, Y. 2000, *A&A*, v. 361, p. 226-230 (2000), 361, 226

Liu, Q.-Y., & Yang, Y.-L. 2003, *ChJAA*, 3, 142

Lucy, L. 1968a, *ApJ*, vol. 151, p. 1123, 151, 1123

—. 1968b, *ApJ*, vol. 153, p. 877, 153, 877

Lucy, L. B. 1967, *Zeitschrift für Astrophysik*, Vol. 65, p. 89, 65, 89

Malkov, O. Y., Oblak, E., Snegireva, E., & Torra, J. 2006, *A&A*, 446, 785

Mestel, L. 1968, *MNRAS*, 138, 359

Mochnacki, S. W. 1981, *ApJ*, Part 1, vol. 245, Apr. 15, 1981, p. 650-670., 245, 650

—. 1984, *ApJSupplement Series* (ISSN 0067-0049), vol. 55, Aug. 1984, p. 551-561., 55, 551

Moss, D. 2004, *MNRAS*, 352, L17

O'Connell, D. 1951, *Riverview College Observatory publications*; v. 2, no. 6= whole no. 10; *Riverview College Observatory publications*; v. 2, no. 6., Riverview, NSW:[Riverview College Observatory, 1951], p. 85-100: ill.; 27 cm., 2, 85

Okamoto, I., & Sato, K. 1970, *Publications of the Astronomical Society of Japan*, 22, 317

Otero, S. A., & Claus, F. 2004, *IBVS*, 5495, 1

Paegert, M., Stassun, K. G., Collins, K. A., et al. 2021, arXiv preprint arXiv:2108.04778

Paki, E., Poro, A., & Moosavi Rowzati, M. D. 2025, *Galaxies*, 13, 74

Palaversa, L., Ivezić, Ž., Eyer, L., et al. 2013, *AJ*, 146, 101

Park, J.-H., Lee, J. W., Kim, S.-L., Lee, C.-U., & Jeon, Y.-B. 2013, *PASJ*, 65, 1

Podsiadlowski, P., Rappaport, S., & Pfahl, E. D. 2002, *ApJ*, 565, 1107

Poro, A., Jahangiri, E., Sarvari, E., et al. 2025a, *MNRAS*, 538, 1427

Poro, A., Li, K., Michel, R., & et al. 2025b, *PASP*, 137, 084201

Poro, A., Paki, E., Alicavus, F., & Michel, R. 2026a, arXiv preprint arXiv:2601.00232

Poro, A., Sarostad, A., Davoudi, M., et al. 2026b, *PASP*, 1, 1. <https://arxiv.org/abs/2602.05038>

Poro, A., Tanriver, M., Michel, R., & Paki, E. 2024a, *PASP*, 136, 024201

Poro, A., Hedayatjoo, M., Nastaran, M., et al. 2024b, *New Astronomy*, 110, 102227

Poro, A., Li, K., Michel, R., et al. 2024c, *AJ*, 168, 272

Poro, A., Baudart, S., Nourmohammad, M., et al. 2024d, *Research in Astronomy and Astrophysics*, 24, 055001

Poro, A., Li, K., Michel, R., et al. 2025c, *AJ*, 170, 214

Poro, A., Li, K., Paki, E., et al. 2025d, *MNRAS*, 537, 3160

Poro, A., Michel, R., Coliac, J.-F., et al. 2025e, *PASP*

Pribulla, T., & Rucinski, S. M. 2006, *The Astronomical Journal*, 131, 2986

Prša, A., & Zwitter, T. 2005, *ApJ*, 628, 426

Prša, A., Conroy, K. E., Horvat, M., et al. 2016, *ApJS*, 227, 29

Pylyser, E., & Savonije, G. J. 1988, *A&A*, 191, 57

Qian, S.-B., Zhu, L.-Y., Liu, L., et al. 2020, *Research in A&A*, 20, 163

Qian, S.-B., Wang, J.-J., Zhu, L.-Y., et al. 2014, *ApJS*, 212, 4

Rahunen, T., & Vilhu, O. 1982, in *International Astronomical Union Colloquium*, Vol. 69, Cambridge University Press, 289–299

Ricker, G. R., Latham, D., Vanderspek, R., et al. 2010, in *American Astronomical Society Meeting Abstracts # 215*, Vol. 215, 450–06

Rucinski, S. 1969, *Acta Astronomica*, Vol. 19, p. 245, 19, 245

Shappee, B. J., Prieto, J., Grupe, D., et al. 2014, *ApJ*, 788, 48

Stassun, K. G., Oelkers, R. J., Pepper, J., et al. 2018, *AJ*, 156, 102

Stepien, K. 2005, arXiv preprint astro-ph/0510464

Szczygiel, D., Socrates, A., Paczynski, B., Pojmanski, G., & Pilecki, B. 2008, arXiv preprint arXiv:0812.3909

Terrell, D., & Wilson, R. 2005, *Zdeněk Kopal's Binary Star Legacy*, 221

Tody, D. 1986, in *Instrumentation in astronomy VI*, Vol. 627, SPIE, 733–748

Tutukov, A., Dremova, G., & Svechnikov, M. 2004, *Astronomy Reports*, 48, 219

Vilhu, O. 1982, *A&A*, vol. 109, no. 1, May 1982, p. 17–22., 109, 17

Wang, J.-M. 1994, *ApJ*, Part 1 (ISSN 0004-637X), vol. 434, no. 1, p. 277–282, 434, 277

Webbink, R. F. 2003, *Contact binaries* (ASP Conf. Ser.)

Wilson, R. 2001, *IBVS*, 5076, 1

Wilson, R. E., & Devinney, E. J. 1971, *ApJ*, vol. 166, p. 605, 166, 605

Yakut, K., & Eggleton, P. P. 2005, *ApJ*, 629, 1055

Yıldız, M., & Doğan, T. 2013, *MNRAS*, 430, 2029

Zhou, D.-Q., & Leung, K.-C. 1990, *ApJ*, 355, 271